UC Berkeley
UC Berkeley Previously Published Works

Title
Elastic anisotropy modeling of Kimmeridge shale

Permalink

Journal

ISSN

Authors
Vasin, Roman N
Wenk, Hans-Rudolf
Kanitpanyacharoen, Waruntorn
et al.

Publication Date
2013-08-01

DOI

Peer reviewed

Elastic anisotropy modeling of Kimmeridge shale

Roman N. Vasin,[1,2] Hans-Rudolf Wenk,[1] Waruntorn Kanitpanyacharoen,[1] Siegfried Matthies,[1,2] and Richard Wirth[3]

[1]   Anisotropy of elastic properties in clay-rich sedimentary rocks has been of long-standing interest. These rocks are cap rocks of oil and gas reservoirs, as well as seals for carbon sequestration. Elasticity of shales has been approached by direct velocity measurements and by models based on microstructures. Here we are revisiting the classical Kimmeridge shale studied by Hornby (1998) by first quantifying microstructural features such as phase volume fractions, grain shapes and grain orientations, and pore distributions with advanced analytical methods and then using this information in different models to explain bulk elastic properties. It is shown that by application of a self-consistent algorithm based on Eshelby's (1957) model of inclusions in a homogeneous medium, it is possible to explain most experimental elastic constants, though some discrepancies remain which may be due to the interpretation of experimental data. Using a differential effective medium approach, an almost perfect agreement with experimental stiffness coefficients can be obtained, though the physical basis of this method may be questionable. The influence of single crystal elastic properties, grain shapes, preferred orientation, and volume and shapes of pores on elastic properties of shale is explored.

Citation: Vasin, R. N., H.-R. Wenk, W. Kanitpanyacharoen, S. Matthies, and R. Wirth (2013), Elastic anisotropy modeling of Kimmeridge shale, *J. Geophys. Res. Solid Earth*, *118*, doi:10.1002/jgrb.50259.

1. Introduction

[2] Shales compose a large part of sedimentary basins. They are cap rocks of hydrocarbon reservoirs [e.g., *Aplin and Larter*, 2005], seals in the context of carbon sequestration [e.g., *Chadwick et al.*, 2004], and repositories for nuclear waste [e.g., *Mallants et al.*, 2001; *Bossart and Thury*, 2007]. Organic-rich shales are also important as source rocks in petroleum formation and occurrence [e.g., *Tissot and Welte*, 1984]. A large volume fraction of shales is composed of phyllosilicates that acquire preferred orientation during sedimentation, compaction, and diagenesis. Shales are among the most anisotropic rocks. Largely because of the significance of anisotropy for seismic prospecting, many studies have been dedicated to quantify the elastic anisotropy of shales. Most important are experiments that investigate elastic wave propagation in different directions [e.g., *Johnston*, 1987; *Hornby*, 1998; *Wang et al.*, 2001; *Pham et al.*, 2002; *Dewhurst and Siggins*, 2006; *Nadri et al.*, 2012].

_____

Additional supporting information may be found in the online version of this article

[1]Department of Earth and Planetary Science, University of California, Berkeley, California, USA.

[2]Frank Laboratory of Neultron Physics, Joint Institute for Nuclear Research, Dubna, Russia.

[3]GFZ – Helmholtz Centre Potsdam, Germany.

Corresponding author: H.-R. Wenk, Department of Earth and Planetary Science, University of California, 495 McCone Hall, Berkeley, CA 94720, USA. (wenk@berkeley.edu)

[3] Elastic anisotropy of shales is directly linked to preferred orientation patterns—textures—of component minerals, especially phyllosilicates [e.g., *Sayers*, 1994; *Johansen et al.*, 2004] that are characterized by high single crystal elastic anisotropy [e.g., *Aleksandrov and Ryzhova*, 1961; *Vaughan and Guggenheim*, 1986; *Manevitch and Rutledge*, 2004; *Suter et al.*, 2007; *Mazo et al.*, 2008a; *Militzer et al.*, 2011]. Another contribution is related to grain shapes and the pore structure, especially flat pores, which, like phyllosilicate minerals, display a preferred orientation pattern. Several investigations have aimed at explaining elastic properties of shales, including self-consistent (SC) or differential effective medium (DEM) approaches [e.g., *Rundle and Schuler*, 1981; *Hornby et al.*, 1994; *Jakobsen et al.*, 2000; *Dræge et al.*, 2006; *Ortega et al.*, 2007; *Bayuk et al.*, 2007; *Nishizawa and Kanagawa*, 2010; *Moyano et al.*, 2012], but these models often use hypothetical assumptions about material properties, preferred orientations, and microstructures. For example, a microstructure-based modeling has been performed by *Hornby et al.* [1994] to explain elastic wave velocities measured by *Jones and Wang* [1981] in a Cretaceous shale. However, this model relies on an arbitrary clay platelet orientation distribution and also assumes isotropic elastic properties for clay minerals.

[4] The Kimmeridge shale [*Hornby*, 1998] is chosen as a sample for this study as it is still one of the few samples for which elastic properties have been determined in detail with ultrasonic velocity measurements. We characterize microstructure of this sample by incorporating advanced X-ray diffraction and imaging methods and latest available data on elastic properties of minerals composing this shale.

[5] The first part provides a short review on general methods of elastic property averaging (section 2). The observed microstructures are the basis for modeling the shale anisotropic elastic properties. For the first modeling approach, we choose a modified version [*Matthies*, 2010] of a classical SC method [e.g., *Kröner*, 1958; *Budiansky*, 1965; *Hill*, 1965] that is based on *Eshelby*'s [1957] solution for ellipsoidal particles (including pores) in a homogeneous medium. The second approach uses a combination of this SC method and a differential effective medium (DEM) approach [*Bruggeman*, 1935] as proposed by *Hornby et al.* [1994].

[6] We quantify the required microstructural information (section 3). With synchrotron X-ray diffraction, it has become possible to determine mineral volume fractions and orientation distributions of complex multiphase rocks [e.g., *Lonardelli et al.*, 2007]. Porosity can be analyzed with X-ray tomography [e.g., *Kanitpanyacharoen et al.*, 2013], and the microstructure and nanostructure, both of minerals and pores, become better defined with transmission electron microscopy. This measured microstructural information is combined with single crystal elastic properties that have become available for phyllosilicates through ab initio calculations [e.g., *Militzer et al.*, 2011] to calculate model bulk elastic properties of shale. Then we compare model results with experimental data (section 4). We pay particular attention to the influence of grain shapes, pore volumes, and pore geometry to understand their influences on elastic properties. Also, we highlight some of the uncertainties in experimental data and model components, as well as simplifications that are currently necessary to apply available methods.

2. General Methods of Elastic Properties Averaging

[7] Linear elastic properties of a material can be described with the twice-symmetric fourth-rank stiffness tensor C_{ijkl} (or compliance S_{ijkl} satisfying the "inversion relation" $C_{ijkl} \equiv S_{ijkl}^{-1}$) that, in most general case, has 21 independent components [e.g., *Nye*, 1985]. Shales are considered transversely isotropic materials [e.g., *Hornby et al.*, 1994; *Hornby*, 1998] as supported by axial symmetry of preferred orientations (fiber textures) and microstructures [e.g., *Wenk et al.*, 2008]. In the case of axial symmetry and a coordinate system with the Z axis parallel to the symmetry axis, there are only five independent elastic tensor components (in standard two-index Voigt notation, they are $C_{11} = C_{22}$, $C_{12} = C_{11} - 2C_{66}$, $C_{13} = C_{23}$, C_{33}, and $C_{44} = C_{55}$; all others are equal to zero).

[8] Commonly elastic properties of polycrystalline aggregates with texture are estimated by averaging single crystal properties over the orientation distribution. This can be done with different models in order to approximate in some way the micromechanical interaction of grains in the solid sample.

[9] The Hooke's law for the single crystal can be written as

$$\sigma_{ij} = {}^{0}C_{ijkl}\varepsilon_{kl},\qquad(1)$$

or in compact form

$$\sigma = {}^{0}C\varepsilon,\qquad(2)$$

where σ is the stress tensor, ε is the strain tensor, and the "0" index denotes single crystal property.

[10] For a polycrystal, an averaging procedure has to be applied and Hooke's law can formally be written as

$$\overline{\sigma} = \overline{C}\,\overline{\varepsilon} = \overline{{}^{0}C\varepsilon},\qquad(3)$$

where the "‾" symbol denotes certain average of corresponding values.

[11] Note that if all constituents of the polycrystalline material are under the same strain, then strain will enter the right side of equation (3) only as a constant multiplier outside of the averaging procedure and

$$\overline{C} = \overline{{}^{0}C}\qquad(4)$$

follows for the elastic properties of polycrystal aggregates. Simple arithmetic averaging can then be applied to single crystal elastic properties, meaning that the elastic tensor of each single crystal grain in the polycrystal with orientation g has to be rotated into the macroscopic sample coordinate system K_A (using an orthogonal transformation tensor $W(g)$ that is related to Euler angles, depending on their definition, and describes the orientation g) [e.g., *Matthies et al.*, 2001, equation 61a] and then weighted by volume fraction occupied by this grain that is equal to the corresponding orientation distribution function (ODF) $f(g)$ value. Then polycrystal elastic properties can be determined as sum, or integral, over all possible grain orientations in orientation space G:

$$^{VOIGT}C = \overline{C_{ijkl}} = {}^{0}C_{stuv}\int_{G} W_{is}(g)W_{jt}(g)W_{ku}(g)W_{lv}(g)f(g)\mathrm{d}g.\qquad(5)$$

[12] This scheme was first introduced and applied to isotropic polycrystals by *Voigt* [1887]. Here, in equation (5), the calculation of multiphase material properties is also possible by additional weighting over volume fractions of corresponding phases.

[13] A similar average can be performed for elastic compliances, assuming equal stresses within each grain [*Reuss*, 1929]:

$$^{REUSS}S = \overline{S_{ijkl}} = {}^{0}S_{stuv}\int_{G} W_{is}(g)W_{jt}(g)W_{ku}(g)W_{lv}(g)f(g)\mathrm{d}g.\qquad(6)$$

[14] As a rule, for crystalline materials, Voigt and Reuss approximations result in different elastic constants:

$$^{REUSS}S \neq (^{VOIGT}C)^{-1},\qquad(7)$$

forming upper and lower "bounds" for the elastic properties of the medium. The difference between these boundaries increases as grain-preferred orientation distributions become closer to random or with increase of elastic anisotropy of single crystals [e.g., *Matthies et al.*, 2001; *Lokajicek et al.*, 2011]. To narrow Voigt-Reuss bounds, an arithmetic average of their results could be used, as proposed by *Hill* [1952]. Hashin-Shtrikman bounds [*Hashin and Shtrikman*, 1963; *Milton and Kohn*, 1988], obtained using a reference medium, are often considered for isotropic multiphase materials [e.g., *Ponte Castañeda and Willis*, 1995; *Arns et al.*, 2002].

[15] There are several simple averaging schemes producing the polycrystalline properties, exactly obeying the "inversion relation" $C \equiv S^{-1}$, e.g., SuperHill [*Matthies et al.*, 2001] that uses a so-called "symmetric square root" operation applied

to both Hill bounds or a geometric mean (GEO) [*Matthies and Humbert*, 1995]:

$$^{GEO}S \equiv \left(^{GEO}C\right)^{-1} = \exp\left(\overline{\ln^0 S}\right), \tag{8}$$

where the averaging procedure of the expression in parentheses over the ODF (or phase volume fractions) is again arithmetic. The geometric mean algorithm also obeys the statistically important "group principle": for any subdivision of a sample into a set of small volumes, the averaging over the total volume is equivalent to the averaging of the averaged values of those small volumes [*Matthies et al.*, 2001].

[16] Such methods generally require only knowledge about ODFs, volume fractions, and single crystal elastic properties of constituent phases and are appropriate for materials with equiaxed grain shapes. But none of these averages is able to take grain size, grain shape, or pore distributions into account. They are reasonably successful in explaining elastic properties of nonporous metals [*Spalthoff et al.*, 1993] and some metamorphic rocks [*Ben Ismail and Mainprice*, 1998], but for shales, calculated elastic properties are always much stiffer than observed properties, and anisotropy is generally lower [e.g., *Valcke et al.*, 2006; *Wenk et al.*, 2008]. A good comparison of Voigt, Reuss, and GEO models, together with experimental data for mica aggregates, is given by *Cholach and Schmitt* [2006].

[17] The grain shape can have a significant impact on bulk elasticity of materials. Thus, for complex materials such as shales, where phyllosilicate grains have a shape of an oblate spheroid (or a "platelet"), a more sophisticated approach is required. To correctly address the problem of stress equilibrium and strain compatibility in heterogeneous materials, finite element methods have been used [e.g., *Makarynska et al.*, 2008; *Srinivasan et al.*, 2008; *Radtke et al.*, 2010] but they are still very difficult to apply to very heterogeneous multiphase materials with complex microstructure and orientation distributions such as shales.

[18] A self-consistent scheme based on *Eshelby*'s [1957] concept of ellipsoidal inclusions in a homogeneous matrix was developed into an iterative procedure, able to compute bulk elastic properties of anisotropic polycrystalline materials [e.g., *Kröner*, 1958; *Kneer*, 1965; *Walpole*, 1969; *Morris*, 1970]. The drawback of this physically reasonable approach is that two iterative procedures, based on averaging of stiffness or compliance, respectively (namely, p the stiffness-related branch, and q the compliance-related branch) [*Morris*, 1970; *Hirsekorn*, 1990], can yield different polycrystal elastic constants, if a nonspherical inclusion (i.e., grain) shape is considered. The p-branch self-consistent (SC) solution is

$$^{i+1}C = {}^iC + {}^ip = {}^iC + \overline{\left(^iC - {}^iE^{-1}\right)\cdot{}^iu}, {}^iC \to {}^{p-branchSC}C \text{ when } i\to\infty, \tag{9}$$

and the q-branch solution is

$$^{i+1}S = {}^iS + {}^iq = {}^iS + \overline{{}^iu\cdot{}^iS}, {}^iS \to {}^{q-branchSC}S \text{ when } i\to\infty, \tag{10}$$

where

$$^iu = \left(^0C - \left(^iC - {}^iE^{-1}\right)\right)^{-1}\cdot{}^iE^{-1} - I, \tag{11}$$

$$^iE = {}^iT\cdot{}^iS, \tag{12}$$

$$I_{ijkl} = \left(\delta_{ik}\delta_{jl} + \delta_{il}\delta_{jk}\right)/2, \tag{13}$$

[19] T is the Eshelby tensor relating stress free and total deformation of elliptical inclusions [*Eshelby*, 1957; *Matthies*

and Vinel, 2005], and δ_{ij} is the Kronecker delta. Once again "0" index denotes single crystal property, and averaging of tensor properties over the ODF and phase volume fractions is performed in a similar manner as in equation (5).

[20] Here we will use this approach but modified by *Matthies* [2010], adding elements of the geometric mean approximation and successfully applied to describe elastic properties of porous polycrystalline graphite [*Matthies*, 2012] and biotite gneiss [*Wenk et al.*, 2012]. In the so-called GeoMIXself (GMS) approximation, the geometric mean enters as symmetric square root [*Matthies et al.*, 2001] applied to results of p- and q-branches after each iteration:

$$^{i,GMS}C \equiv {}^{i,GMS}S^{-1} = SQRT^{SYM}\left(^iC\cdot{}^iS^{-1}\right)$$

$$= {}^iC^{1/2}\cdot\left(^iC^{-1/2}\cdot{}^iS^{-1}\cdot{}^iC^{-1/2}\right)^{1/2}\cdot{}^iC^{1/2}. \tag{14}$$

[21] Thus, the GMS algorithm converges to only one solution for bulk elastic properties of polycrystals, obeying the "inversion relation." Generally, pores or cracks can be introduced into the medium as "empty" grains, i.e., with elastic tensor $^0C \equiv 0$. Fluid filled pores will have the shear components of the corresponding ^0C equal to zero. Current realization of GMS algorithm (the "GeoMIXself4" Fortran-based program) allows textures of different phases to be entered in form of discrete distribution functions with $5° \times 5° \times 5°$ resolution, effectively resulting in ≈ 200000 unique orientations for each phase, for triclinic crystal and sample symmetry. Since nonspherical grain shapes could be considered, it is possible to perform averaging procedures in equations (9) and (10) using shape orientation distribution functions (SODF) $F(\Omega)$ instead of ODFs $f(g)$. In this case, the crystal lattice orientation is considered to be "fixed" in each ellipsoidal grain according to certain rules describing their relative orientation.

[22] We should highlight non-obvious characteristics of the GMS approximation. First, it considers a macroscopic system with practically infinite (or at least very large) number of grains and thus is "dimensionless," i.e., the ellipsoidal grain shape with axes $\{a_1, a_2, a_3\}$ is equivalent to $\{1, a_2/a_1, a_3/a_1\}$, etc. Second, no correlations between grain positions are taken into account (as the ODF is not a correlation function). Third, all the "infinite" volume of the macroscopic material should be filled by grains, without any gaps or overlaps. This automatically leads to the conclusion that the GMS approximation virtually considers the distribution of the grains on size. For example, to fill the 3-D volume with spheres without gaps, one has to assume a power law size distribution $\sim R^{-\alpha}$; R are the sphere's radii and α is close to 3 for the disordered packing [*Aste*, 1996].

[23] Macroscopic (or "effective") elastic constants are calculated by the GMS algorithm. Thus, it is applicable in the so-called "long-wave" approximation [e.g., *Berryman*, 1980a, 1980b; *Schoenberg and Douma*, 1988]. Ultrasonic wave velocities can be described by these elastic constants only if the wavelength is much longer than the size of material heterogeneities (grains, cracks, and pores). If the wavelength is comparable or shorter than the size of heterogeneities, wave field patterns and elastic wave velocities may differ considerably from those corresponding to "effective" elastic constants [e.g., *Mukerji et al.*, 1995; *Liu and Schmitt*, 2006; *Silva and Stovas*, 2009].

Table 1. Mineral Composition of Kimmeridge Shale[a]

Mineral	This Study (vol %)	This Study (wt %)	Hornby [1998] (wt %)
Quartz	25.1	23.6	30
Albite	3.7	3.4	5
K-feldspar	-	-	2
Pyrite	4.4	7.8	4
Kaolinite	8.9	8.0	22
Illite-smectite	29.9	29.3	35[b]
Illite-mica	28.0	27.9	[b]
Chlorite	-	-	2

[a]Columns 2 and 3 are the results of Rietveld refinement of synchrotron diffraction images; column 4 is an excerpt from *Hornby* [1998, Table 2].
[b]*Hornby* [1998] gives only the total amount of illite-smectite and illite-mica in the sample.

[24] In order to apply the GMS approximation to the full extent, microscopic and macroscopic sample characteristics have to be known: (1) single crystal stiffness constants ^0C, (2) volume fractions of minerals and pores/cracks, (3) the orientation distributions $f(g)$ of the minerals, (4) mass densities ρ that determine the density of the sample, (5) grain shapes and pores/cracks geometry approximated by ellipsoids, and (6) shape orientation distribution functions $F(\Omega)$ for grains as well as for this cracks and pores.

[25] Here we will use modern experimental methods and recent literature data to obtain the best available quantitative information for this Kimmeridge shale. In the next section, we will describe microstructural features.

3. Microstructural Information About Kimmeridge Shale

3.1. Sample and Analytical Methods

[26] The sample of blackish Kimmeridge shale was obtained from a borehole in the North Sea at 3750 m below sea level and has been described by *Hornby* [1998]. The mineralogical composition was originally determined with infrared spectrometry and X-ray powder diffraction (Table 1). A porosity of 2.5 % was determined by helium expansion, and an average matrix density (of only crystalline part, without pores) of 2.69 g/cm^3 was established, based on the mineral analysis.

[27] A piece of this sample was reanalyzed as a part of this investigation. Methods used are scanning electron microscopy (SEM), transmission electron microscopy (TEM), synchrotron X-ray diffraction, and X-ray microtomography. Details about the methods have been published elsewhere, and here we will only give brief summaries. For the following experimental methods, a piece of the sample was impregnated and mechanically stabilized with Epoxy and then cut with a diamond saw and kerosene as a cooling agent into slices.

[28] For the SEM, a slice of the shale sample was polished and carbon coated and examined with a Zeiss Evo MA10 variable vacuum SEM, equipped with an EDAX energy-dispersive spectroscopy (EDS) system at UC Berkeley.

[29] TEM analyses were performed using a FEI Tecnai G2 X-Twin transmission electron microscope equipped with a Gatan Tridiem energy filter and a Fishione high-angle annular darkfield detector at GFZ – Helmholtz Centre Potsdam. To exclude preparation-induced damage, the samples for

TEM studies were prepared with a focused ion beam (FIB) device (FEI FIB200TEM) at GFZ [*Wirth*, 2009].

[30] For microtomography experiments, a small prism was cut and ground to a cylinder 1 mm in diameter and 5 mm in length. The cylinder was investigated with synchrotron X-ray radiation tomography at three facilities, the TOMCAT (tomographic microscopy and coherent radiology experiments) beamline of the Swiss Light Source (SLS) at the Paul Scherrer Institute in Villigen, Switzerland, beamline 8.3.2 of the Advanced Light Source at Lawrence Berkeley National Laboratory, and beamline 2-BM-B of the Advanced Photon Source (APS) at Argonne National Laboratory. This sample was also used as a round robin to compare resolution of the facilities, and methods are described in detail by *Kanitpanyacharoen et al*. [2013].

[31] The hard X-ray synchrotron diffraction measurements were done at beamline BESSRC 11-ID-C of APS [e.g., *Wenk et al*., 2010]. A monochromatic X-ray beam with a wavelength of 0.10798 Å and a beam diameter of 1 mm was used. Diffraction images were recorded with a Perkin Elmer amorphous silicon detector (2048 × 2048 pixels) mounted at a distance of about 180 cm away from the sample. The sample is a 1 mm thick slab mounted on a goniometer perpendicular to the incident beam and was rotated in 15° increments around the normal to the bedding plane from −45° to +45°. At each rotation position, a diffraction image was recorded while the sample was translated 2 mm parallel to the rotation axis to obtain a representative volume average. The rotations are necessary to obtain adequate pole figure coverage for determining preferred orientation.

3.2. Scanning Electron Microscopy (SEM) Results

[32] An intermediate magnification backscattered electron (BE) image illustrates a complex microstructure with almost horizontal layering (Figure 1). The bright spherical particles are pyrite. Then there are black regions of more complex shape, some flat and others more equiaxed. These are pores. Most of these are intrinsic, as confirmed by TEM images,
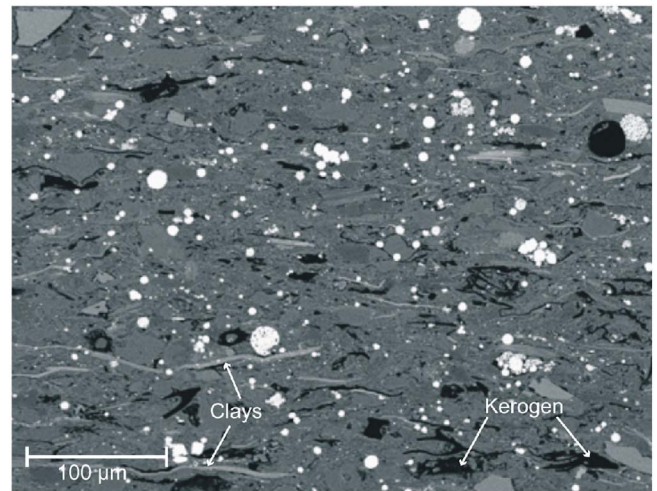

Figure 1. SEM-BE image illustrating microstructure of Kimmeridge shale. Bent platelets are detrital illite-mica (arrows), defining the bedding plane. Pores and kerogen structures (arrows) are black. Framboidal aggregations of pyrite are white. Angular fragments are quartz and feldspar.
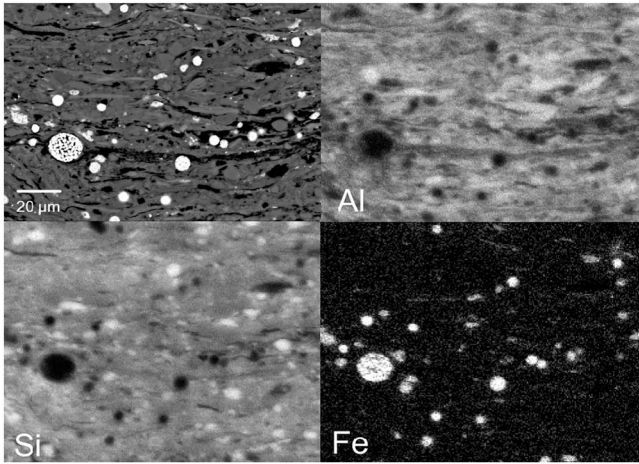
4

Figure 2. Higher magnification SEM-BE image with a framboidal aggregation of pyrite and EDS maps of the Al, Si, and Fe distributions. Note the variation of Fe content of phyllosilicate platelets.

but a few may be artifacts created during sample preparation such as the big round hole on the right side of the image next to a framboidal pyrite aggregate. Some pores show a complex structure and are filled with kerogen (see arrows on the lower right corner of Figure 1). Angular gray fragments are quartz (e.g., upper left corner) and most of the remainder are phyllosilicates. Among phyllosilicates, there are large platelets, generally slightly bent (some indicated as clays

in Figure 1). These are detrital illite-mica. Different gray shades indicate variations in composition. Some mica corresponds to muscovite (darker shades), but other platelets contain significant amounts of iron and magnesium and may be trioctahedral (lighter shades). Figure 2 shows a region with higher magnification. The BE image displays again detrital mica but also more fine-grained authigenic sheet silicates. On elemental maps of Al, Si and Fe quartz and some feldspar fragments can be identified. Al and Fe maps document considerable chemical variation in the composition of phyllosilicates.

[33] From the SEM image of Figure 1, grain and pore shapes can be quantified. The shape of clay platelets can be approximated by oblate spheroids with axes {1:1:ζ}; $\zeta \leq 1$. Figure 3a shows a histogram distribution of grain aspect ratios, averaging to $\zeta \approx 0.05$, and Figure 3b the corresponding distribution of aspect ratios for pores. There is a significant number of high aspect ratio pores ($\zeta \approx 0.5-1$), as well as low aspect ratio pores ($\zeta \approx 0.01-0.03$). It is evident that detrital illite is aligned, and low aspect ratio pores are often associated with illite platelets.

3.3. Transmission Electron Microscopy (TEM) Results

[34] TEM images reveal considerable structural complexities at the nanometer scale. Figure 4a shows a typical bright-field image with phyllosilicate platelets warping around a quartz fragment. Nanopores (white) are aligned parallel to the platelets and have low aspect ratios. Phyllosilicates have similar orientations with a variation of about 30°. Figure 4b shows a region with dominantly authigenic phyllosilicates
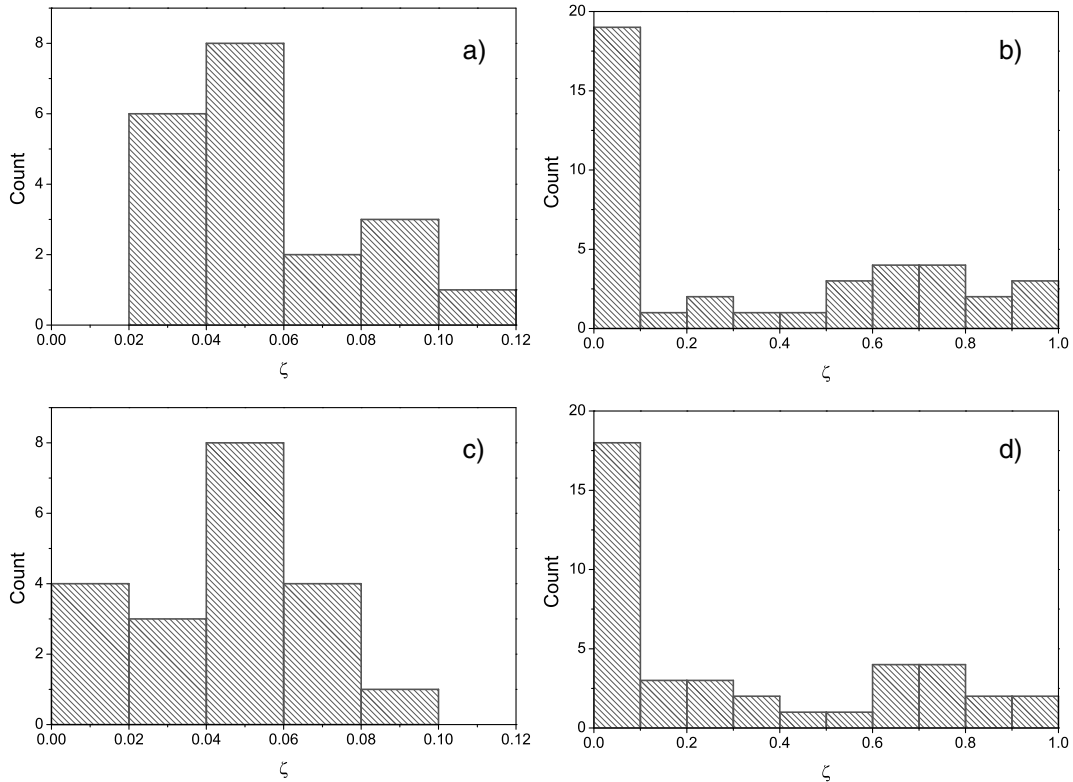

Figure 3. Histogram distributions of aspect ratios ζ based on electron microscope images. (a) SEM, detrital illite grains; (b) SEM, high and low aspect ratio pores; (c) TEM, authigenic phyllosilicates grains; and (d) TEM, high and low aspect ratio pores.
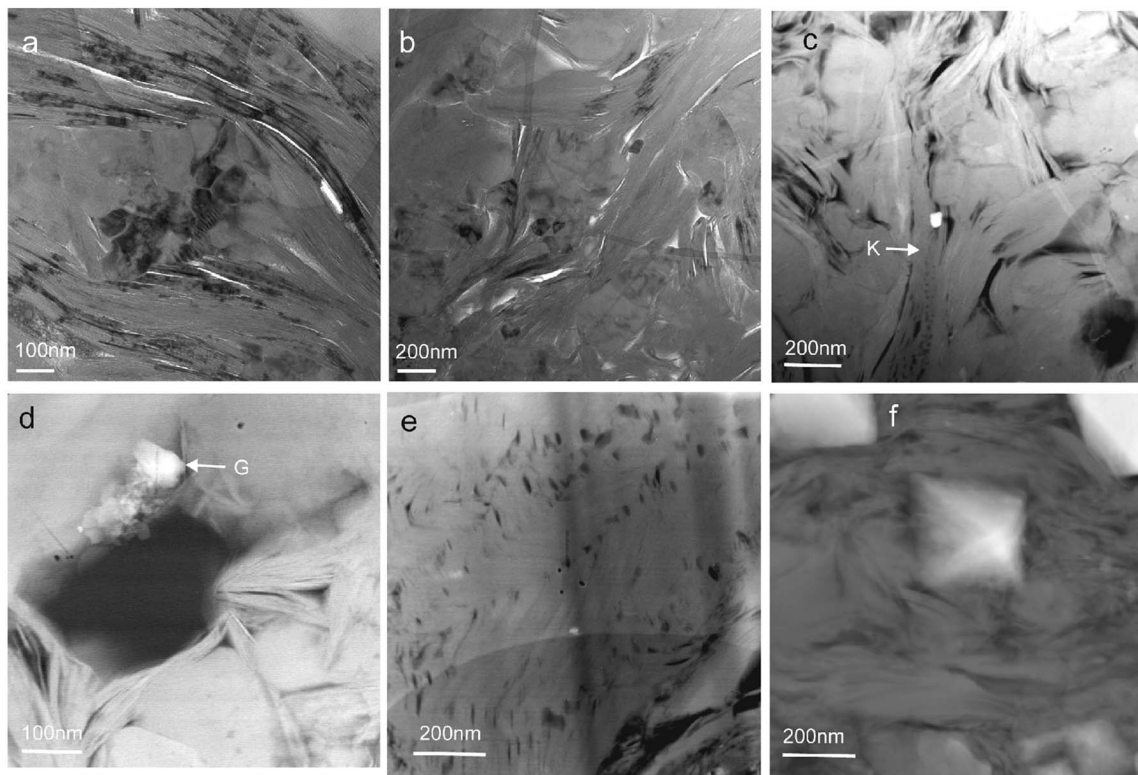
5

Figure 4. TEM images of Kimmeridge shale. (a) Quartz aggregation surrounded by illite-mica platelets, (b, c) heterogeneous region with illite-smectite and kaolinite (K, arrow), (d) equiaxed pore with authigenic illite-smectite and gypsum (bright, G, arrow), (e) kinked illite with nanopores aligned along kink plane, and (f) pyrite octahedra surrounded by illite-smectite crystallites. Bright-field images are shown in Figures 4a and 4b and high-angle annular darkfield images in Figures 4c–4f.

with a much higher dispersion in orientations, both of grains and flat pores. In a darkfield image (DF), kaolinite can be identified based on chemical composition and diffraction pattern (Figure 4c). Kaolinite crystallites are stacked between illite-smectite (shown by arrow). Figure 4c also shows considerable dispersion of grain orientations compared with Figure 4a. Another DF image shows an example of an equiaxed nanopore (dark, Figure 4d) surrounded by illite-smectite as well as gypsum (white). Detrital illite-mica is generally bent and occasionally kinked (Figure 4e). Along kink planes, there is abundant nanoporosity. Pyrite is often euhedral, with octahedral shape (Figure 4f), compared with framboidal aggregations in Figures 1 and 2.

[35] Aspect ratios for phyllosilicate platelets and pores have also been quantified, based on TEM images (Figures 4a–4c and 4f) and are represented in histograms (Figures 3c and 3d). Distributions are similar as those derived from SEM images. Thus, both TEM and SEM suggest that grain shapes of phyllosilicates are oblate spheroids with average axes ratio {1:1:0.05}, while quartz, pyrite, and plagioclase grains are equiaxed.

[36] High-resolution images of illite-smectite display fringes of ≈1 nm thickness corresponding to the mica lattice spacing (Figure 5a), but with abundant irregular stacking faults every few unit cells, interrupting the lattice structure. There is no evidence for ordered polytypism. This stacking disorder is expressed by diffuse streaks in the diffraction pattern obtained by Fourier transform (Figure 5b).

3.4. Synchrotron X-ray Microtomography Results

[37] The 3-D structure of micropores has been investigated by X-ray microtomography measurements and is illustrated in Figure 6a [*Kanitpanyacharoen et al.*, 2013]. Pores are mostly platelet shaped and aligned roughly parallel to the bedding plane. Spherical pores are also present and dispersed throughout the sample, while a few large fractures are observed in some areas (not shown). Based on 3-D tomography, the total fraction of low-density features (including empty and water-filled pores and kerogen) is estimated at 6.3 vol %. Since the resolution of X-ray microtomography is in the range of 1 μm, the microporosity visible in Figure 6a does not include nanoporosity which has been documented in TEM images (Figure 4). This infers that porosity of 6.3% is lower than actual porosity of the material. It also should be noted that X-ray tomography was done on a small cylindrical sample and results could suffer from sample heterogeneities, e.g., local kerogen networks as illustrated in Figure 6b.

3.5. Synchrotron X-ray Diffraction Results

[38] For estimation of mineralogical composition and preferred orientations, we relied on the Rietveld refinement of synchrotron X-ray diffraction images, implemented in the software MAUD [*Lutterotti et al.*, 1997]. The Rietveld method [*Rietveld*, 1969] obtains a best fit between measured diffraction patterns and a model, based on a number of refined parameters, such as phase volume fractions, unit cell
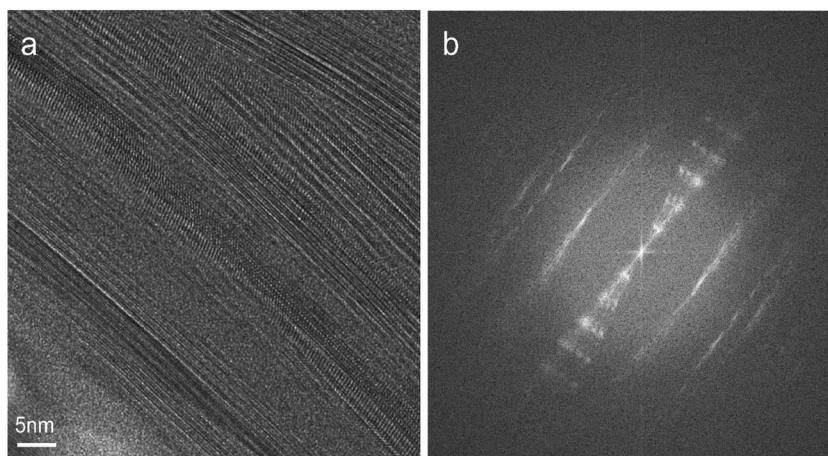
Figure 5. (a) High-resolution bright-field image with basal 1 nm lattice planes of illite, illustrating irregularities and porosity (bright) at the nanoscale. (b) Corresponding Fourier transformation displaying bending and stacking disorder.

parameters, and preferred orientations. The Kimmeridge shale has been used as an example for a tutorial that describes the analytical procedure in detail, though in the tutorial some simplifications were made [*Wenk et al.*, 2013]. As described in section 3.1, seven diffraction images, measured at different sample tilts, were used and integrated over 10° sectors to obtain diffraction patterns. For the Rietveld analysis, a scattering angle 2θ range from 0.4° to 4.3° was applied. A polynomial function with five coefficients was used to refine the background of each image. Six mineral phases were considered, with corresponding crystallographic information from the literature: kaolinite [*Bish and Von Dreele*, 1989; amcsd #0012232], illite-muscovite [*Gualtieri*, 2000; amcsd #0012865], illite-smectite modeled after phengite [*Plançon et al.*, 1985], quartz [*Antao et al.*, 2008; amcsd #0006212] with structure adjusted to left-handed quartz, pyrite [*Rieder et al.*, 2007; amcsd #0012728], and albite [*Downs et al.*, 1994; amcsd #0001683]. For the purpose of this study, the composition was slightly simplified by omitting minor phases such as K-feldspar and chlorite with contributions of < 2 vol %. Illite-muscovite with a cell parameter of 20 Å was chosen for detrital mica, though some of the mica is trioctahedral. The illite-smectite structure is interrupted by stacking faults as revealed by TEM (Figure 5). This stacking disorder was taken into account with the *Ufer et al.* [2004] model implemented in MAUD [*Lutterotti et al.*, 2010]. There are various feldspars present in small amounts. We use albite and only refine its volume fraction.

[39] Only phyllosilicates display significant preferred orientation, and textures of quartz, pyrite, and albite were considered to be random. The E-WIMV model [*Matthies*, 2002; *Lutterotti et al.*, 2004] with a 10° resolution was used to refine phyllosilicate ODFs, with and without imposing axial symmetry around the bedding plane normal. The 3-D ODFs were exported from MAUD in a standard $5° \times 5° \times 5°$ grid, smoothed with a 7.5° Gaussian filter in the BEARTEX package [*Wenk et al.*, 1998] and used to calculate pole figures and physical properties. In all the texture-related calculations, the first setting for monoclinic crystals has to be used, i.e.,

(100) is the cleavage plane of illite instead of the more familiar second setting with (001) as the cleavage plane [*Matthies and Wenk*, 2009]. To be consistent with calculations of elastic properties, we will keep this notation for monoclinic phases —illite-mica and illite-smectite—throughout this paper.

[40] Results of Rietveld refinements of Kimmeridge shale were reported earlier [*Wenk et al.*, 2010; *Militzer et al.*, 2011]. The data presented here rely on new measurements with larger sample translation to obtain a better volume average and a more sensitive X-ray detector. Also, Rietveld refinement procedures have improved.
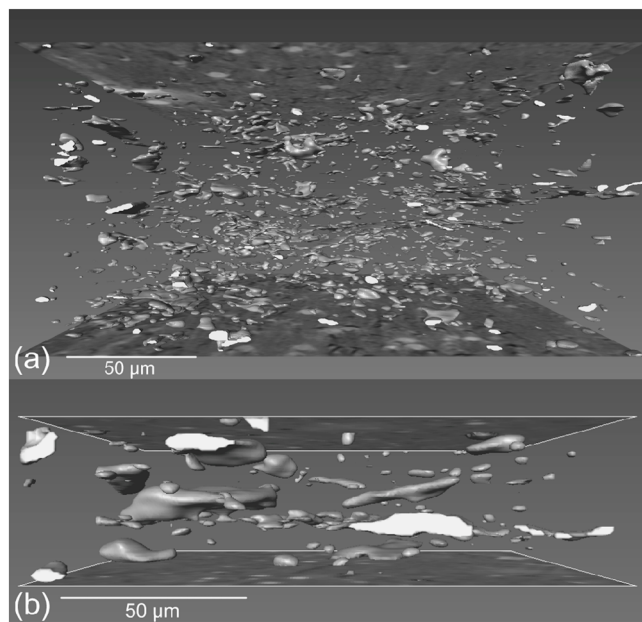

Figure 6. 3-D X-ray microtomography images showing low-density features distribution in Kimmeridge shale. Bedding plane is horizontal. (a) Larger volume with pores and (b) details with kerogen clusters.
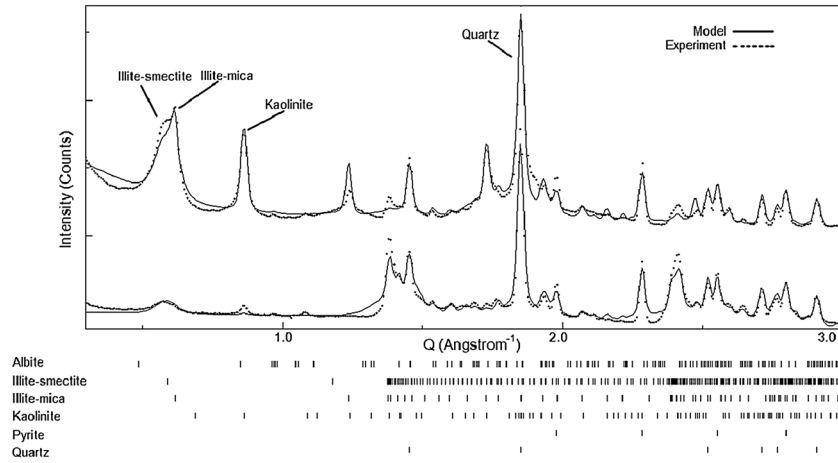
Figure 7. Synchrotron diffraction spectra (intensity versus scattering vector $Q = 2\pi/d$) of Kimmeridge shale obtained by integration of 2-D diffraction images in 10° sectors. (top) Scattering vectors are perpendicular to bedding plane; (bottom) scattering vectors are parallel to bedding plane. Ticks below spectra show positions of diffraction peaks of different minerals. Dots are measured data and solid line is Rietveld fit.

[41] Mineral volume fractions (Table 1) are somewhat different from the analysis reported by *Hornby* [1998] based on Fourier transform infrared spectrometry, but overall they are comparable. Our synchrotron data analysis suggests much less kaolinite and more illite in the sample, which is also supported by SEM/TEM observations. Overall, values of weight fractions of phyllosilicates in the sample are close. Some of the differences can conceivably be attributed to sample heterogeneity, but analytical techniques have considerably improved and we thus rely on the new diffraction data.

[42] Figure 7 illustrates two diffraction spectra, one with the bedding plane horizontal (scattering vectors are close to the bedding plane normal) and one with the bedding plane perpendicular (scattering vectors are in bedding plane). Scattering vector Q ($Q = 2\pi/d$, d is the lattice spacing) is used as scale to make it independent of wavelength. The fit is very good and intensity differences of some diffraction peaks, such as 100 illite and 001 kaolinite, are indicative of strong preferred orientation. With the Rietveld method, we can separate the overlapping diffraction peaks of illite-mica and
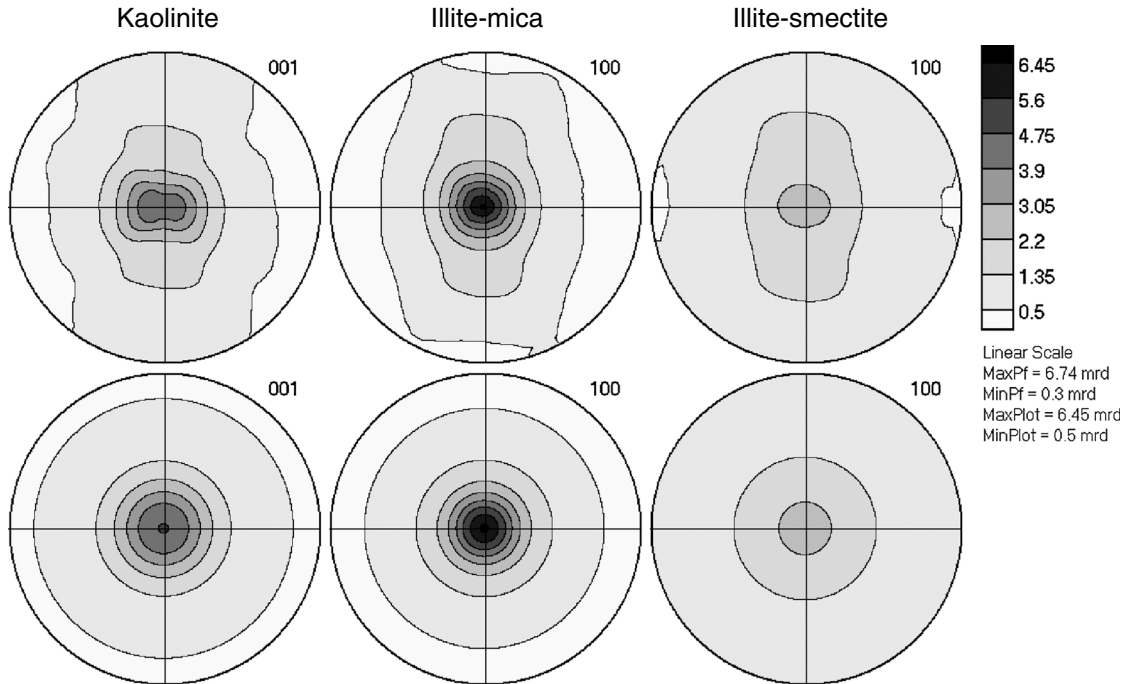

Figure 8. Pole figures of kaolinite, illite-mica, and illite-smectite: (top) without imposing sample symmetry and (bottom) with fiber symmetry imposed. Equal area projections onto the bedding plane and linear scale contours in multiples of a random distribution (m.r.d.).
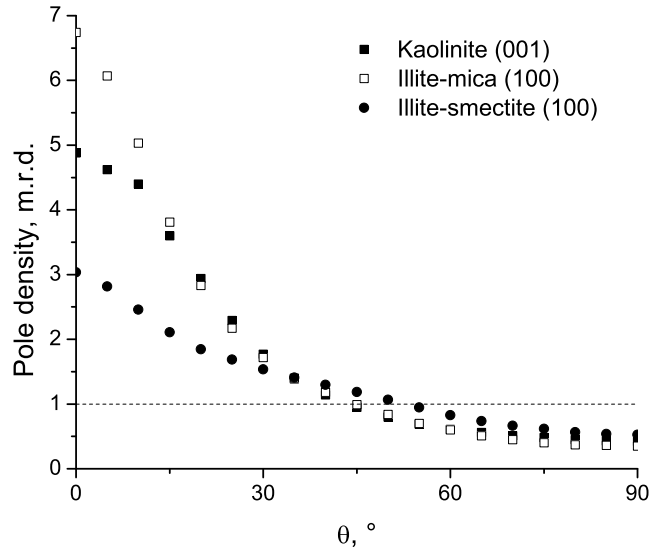
Figure 9. Pole density profiles (001) of kaolinite, (100) of illite-mica, and (100) of illite-smectite (Figure 8, bottom) as function of angle θ with the bedding plane normal. Random orientation distribution is shown as a dashed line.

illite-smectite at $Q \approx 0.6 \, \text{Å}^{-1}$ to perform a quantitative phase and texture analysis.

[43] In a first round of refinements, no sample symmetry was imposed. The (100) pole figures of illite-mica and illite-smectite and (001) pole figure of kaolinite, projected on the bedding plane, show a maximum perpendicular to the bedding plane (Figure 8, top). Pole densities are normalized and expressed in multiples of a random distribution (m.r.d.). Each pole figure is different, but they all display roughly axial symmetry about the bedding plane normal. Minor deviations from axial symmetry are attributed to incomplete pole figure coverage. Thus, in a second round of refinements, axial symmetry was imposed (Figure 8, bottom). In this case, textures can be represented as pole density profiles from perpendicular to parallel to the bedding plane (Figure 9). In texture profiles, the difference of the three minerals is evident, including the full width at half maximum (FWHM) which is about 36° for illite-mica, and is about 57° for illite-smectite, as measured on Figure 9. Illite-mica has the sharpest preferred orientation, which is in agreement with SEM and TEM results.

[44] Table 2 contains characteristic parameters on preferred orientations. A measure of the "sharpness" of an ODF is the "texture index" F_2 [*Bunge*, 1982] which is the integral of the squared ODF $f(g)$ over the orientation space. For the isotropic case, $F_2 = 1$; in the case of single crystal, $F_2 = \infty$. Additional numerical characteristics of the ODF could be assessed by construction of ODF histograms and ODF spectra [*Matthies*, 2005]. The $F_{>1}$ texture parameter gives a measure of the "truly textured" volume part of the crystallites (with ODF values > 1). The parameter PG(>1) describes the fraction of the G-space occupied by these "truly textured" crystallites. From Table 2, it is evident that only a fraction of phyllosilicate crystallites is "textured" (0.2-0.34) which is also seen in the TEM images (Figure 3). A large volume fraction of phyllosilicates (up to 0.42 in case of illite-smectite) is randomly oriented (as indicated by f_{min} value).

3.6. Consideration of Crystallographic and Shape Orientation Distributions Relations for Phyllosilicates

[45] Based on synchrotron diffraction images, ODFs $f(g)$ of three phyllosilicate phases have been calculated and values are stored in $5° \times 5° \times 5°$ Euler angle arrays. These angles relate orientations of the right-handed Cartesian crystal coordinate system K_B ($X_B Y_B Z_B$) of the crystallite with a macroscopic (also right-handed Cartesian) sample coordinate system K_A ($X_A Y_A Z_A$) according to fixed rules [*Matthies et al.*, 1988]. The shape orientation distribution function (SODF) $F(\Omega)$ of platelet-shaped phyllosilicate grains is not measured directly, but it is possible to deduce it from ODF $f(g)$ based on information about the crystal structure, cleavage, and morphology. It is known that mica-type minerals display a characteristic morphology with (001) platelets [e.g., *Bailey*, 1984]—or (100) if monoclinic first setting is used for the crystal. The platelet-shaped grains of phyllosilicates should be parallel to (001) planes for kaolinite and (100) for illite-mica and illite-smectite. It is reasonable to set axes of the grain coordinate system K_E ($X_E Y_E Z_E$) parallel to the axes of ellipsoidal grain. Let three Euler angles {$\alpha_{BE}, \beta_{BE}, \gamma_{BE}$} describe the orientation of K_B in K_E in the same manner that {α, β, γ} describes orientation of K_B in the macroscopic sample coordinate system K_A (using the convention of *Matthies et al.* [1988] for Euler angles). The transformation $K_E \rightarrow K_B$ is performed

Table 2. Information About Preferred Orientations of Phyllosilicates[a]

Mineral	f_{min}	f_{max}	F_2	$F_{>1}$	PG(>1)	FWHM (deg)
Kaolinite	0.19	5.67	1.86	0.32	0.29	45
Illite-mica	0.25	6.74	2.09	0.34	0.29	36
Illite-smectite	0.42	3.04	1.26	0.20	0.39	57

[a]Minimum and maximum ODF values (f_{min} and f_{max}), texture index F_2, "truly textured" volume part of the crystallites $F_{>1}$, part of orientation G-space occupied by these crystallites PG(>1), and FWHM of the pole density distribution on the pole figure of cleavage plane normals (Figure 9).
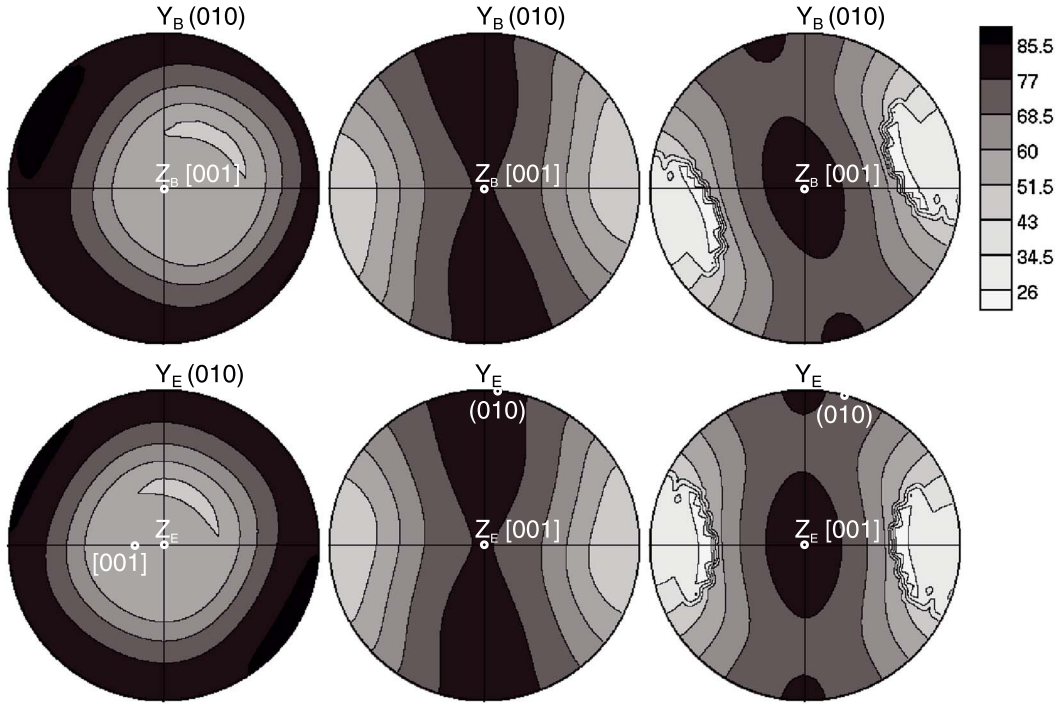
Figure 10. Quasi-longitudinal wave velocities [×100 m/s] for single crystals of kaolinite (left), illite-mica (center), and illite-smectite (right). Equal area projections onto the XY plane of the coordinate system and linear scale contours. Z axis of the coordinate system is in the center of the projection, and X axis is left to right. (top) K_B coordinate system (standard convention) and (bottom) K_E coordinate system. Refer to sections 3.6 and 3.7 for the conventions on choosing crystal coordinate system K_B and grain coordinate system K_E.

by the rotation on $\{\alpha_{BE}, \beta_{BE}, \gamma_{BE}\}$, and considering this additional rotation in the ODF $f(g)$, we have computed SODFs $F(\Omega)$ for all phyllosilicate phases, representing them in $5° \times 5° \times 5°$ arrays.

[46] For the first monoclinic setting, the [001] direction (translation c) is the Z_B axis of the crystal coordinate system and the [100] direction (translation a) is the X_B axis of the crystal coordinate system according to K_B conventions [*Matthies et al.*, 1988]. The X_E axis of the grain coordinate system is normal to the (100) plane. The angle between X_B and X_E is $\Delta = \gamma - 90°$ (where γ is the cell angle). If we consider the grain shape to be that of an oblate spheroid, it is always possible to choose $Z_B \parallel Z_E$. Then for illite-mica and illite-smectite, rotations $\{\alpha_{BE}, \beta_{BE}, \gamma_{BE}\}$ will take the form of $\{\Delta, 0°, 0°\}$. Based on cell parameters given in *Militzer et al.* [2011], necessary rotations are (rounded to whole degrees) $\{-5°, 0°, 0°\}$ for illite-mica and $\{-15°, 0°, 0°\}$ for illite-smectite. Similar rotations can be applied for triclinic kaolinite with a (001) cleavage plane. Using cell parameters from *Militzer et al.* [2011], they are $\{0°, -15°, 0°\}$.

3.7. Single Crystal Elastic Properties

[47] Single crystal elastic properties are a very important part of the model. For quartz we use stiffness coefficients measured by *Heyliger et al.* [2003], for pyrite those derived by ab initio calculations [*Le Page and Rodgers*, 2005], and for triclinic albite experimental data by *Brown et al.* [2006].

[48] There are considerable experimental difficulties related with direct measurements of elastic properties of clay minerals. Thus, for fine-grained kaolinite, illite-mica, and illite-smectite, we relied on ab initio calculations for "perfect"

structures. We used values calculated with a local density approximation by *Militzer et al.* [2011, bold font in their tables]. Density values for all minerals are also taken from corresponding references, and all the used elastic constants and density values used here are listed in Table S1 in the supporting information in two-index form, using the standard Voigt notation.

[49] Prior to performing any ODF-weighted averaging operations, we have to transform all tensors into the same crystal coordinate system that is used for the ODF. For triclinic albite, *Brown et al.* [2006] use the Cartesian coordinate system with the y axis parallel to the crystal translation b, the x axis parallel to $a*$ (perpendicular to b and c), and the z axis forming a right-handed coordinate system. This needs to be converted to the standard convention with the Z_B axis of crystal coordinate system K_B parallel to the crystal c axis [001], the Y_B axis perpendicular to c and a, and the X_B axis forming a right-handed coordinate system [*Nye*, 1985; *Matthies et al.*, 1988]. Also, since texture analysis conventions require that the first setting of crystal coordinate system is used for the monoclinic crystals, C_{ij} stiffness values from *Militzer et al.* [2011] need to be transformed to the first setting [*Matthies and Wenk*, 2009].

[50] Additional rotations are needed to account for the platelet morphology of phyllosilicates grains and inclination of the crystal coordinate system K_B with respect to the grain shape coordinate system K_E. To perform SODF $F(\Omega)$ weighted averaging, elastic tensors of phyllosilicates have to be rotated to K_E. This is done in the same manner as described in section 3.6 for calculation of $F(\Omega)$: for kaolinite

Table 3. Components of Stiffness Tensors C_{ij} [GPa] (Rounded to Second Decimal Digit) for Phyllosilicates in Grain Coordinate System K_E[a]

Mineral	Kaolinite			Illite-mica			Illite-smectite		
Variant	Dry	DEM, 0.05 water content in unit	DEM, 0.127 water content in unit	Dry	DEM, 0.05 water content in unit	DEM, 0.127 water content in unit	Dry	DEM, 0.05 water content in unit	DEM, 0.127 water content in unit
C_{11}	187.42	163.48	130.96	60.14	26.32	13.96	25.15	16.54	10.79
C_{12}	70.41	59.71	46.05	25.55	13.10	8.35	5.89	5.43	4.93
C_{13}	4.84	5.52	5.33	23.97	12.44	8.04	2.43	3.52	3.98
C_{14}	−2.24	−0.49	−0.13	0.00	0.00	0.00	0.00	0.00	0.00
C_{15}	1.24	0.23	0.06	0.00	0.00	0.00	0.00	0.00	0.00
C_{16}	−7.51	−6.32	−4.72	0.03	0.00	0.00	0.60	0.07	0.01
C_{22}	179.70	156.76	125.86	184.36	158.13	127.21	170.58	150.30	121.94
C_{23}	5.89	5.70	5.36	52.93	43.87	34.64	27.87	25.47	21.97
C_{24}	−3.31	−0.73	−0.20	0.00	0.00	0.00	0.00	0.00	0.00
C_{25}	0.03	0.00	0.00	0.00	0.00	0.00	0.00	0.00	0.00
C_{26}	0.78	0.56	0.38	−5.02	−0.79	−0.20	0.16	0.03	0.01
C_{33}	83.91	29.33	14.56	170.00	146.65	118.57	188.50	164.83	132.59
C_{34}	−2.99	−0.26	−0.04	0.00	0.00	0.00	0.00	0.00	0.00
C_{35}	−2.88	−0.21	−0.03	0.00	0.00	0.00	0.00	0.00	0.00
C_{36}	0.73	0.12	0.02	3.97	0.63	0.16	−2.13	−0.41	−0.11
C_{44}	13.52	3.14	0.97	70.42	61.51	49.45	60.34	52.79	42.88
C_{45}	−0.23	−0.06	−0.02	2.75	0.48	0.13	−2.52	−0.98	−0.33
C_{46}	−0.59	−0.13	−0.03	0.00	0.00	0.00	0.00	0.00	0.00
C_{55}	16.04	3.34	1.00	18.48	3.42	1.00	5.46	2.25	0.86
C_{56}	−0.94	−0.18	−0.05	0.00	0.00	0.00	0.00	0.00	0.00
C_{66}	61.08	53.96	43.97	22.15	3.68	1.06	17.49	3.36	1.00

[a]First monoclinic setting is used for illite-mica and illite-smectite. The single crystal (dry) is compared with two DEM models (see section 4.6). Starting water content in DEM procedures is 50%, grain shape is {1:1:0.05}, and associated water-filled pore shape is {1:1:0.01}.

rotations are $\{\alpha_{BE}, \beta_{BE}, \gamma_{BE}\} = \{0°, -15°, 0°\}$, for illite-mica (muscovite) $\{-5°, 0°, 0°\}$, and for illite-smectite $\{-15°, 0°, 0°\}$. The influence of these rotations on the quasi-longitudinal phase elastic wave velocity V_P patterns is shown in Figure 10. It is evident that rotation to K_E brings the maximum V_P values into the projection plane (that is, the phyllosilicate platelet plane). Stiffness coefficients of phyllosilicates in the K_E coordinate system are listed in Table 3.

3.8. Experimental Elastic Properties and Density of Kimmeridge Shale

[51] *Hornby* [1998] determined compressional and shear wave velocities in three different directions and at different pressures with ultrasonic waves (500 and 250 kHz; wavelength is ∼ 1 cm). Here, for comparison with models, we used reported values at pressure of 80 MPa, where porosity should be minimal and particularly "empty" pores and cracks are largely closed. The set of experimental stiffness coefficients $^{exp}C_{ij}$ have been derived by *Hornby* [1998] by fitting experimental ultrasonic velocity data (listed in his Table 5) using Christoffel equations which, in general case, is a complicated procedure [e.g., *Klíma*, 1973; *Jech*, 1991]. Assuming transverse isotropy (axial symmetry) of the Kimmeridge shale, all five independent stiffness components have been calculated with good precision. There is an issue that should be assessed with care in ultrasonic experiments: whether group or phase wave velocities are measured, as the Christoffel equation solution provides phase velocities. Group and phase velocity values parallel to the symmetry axis, and also in the bedding plane of the transversely isotropic shale coincide, but off-axial phase and group velocities (e.g., in the direction tilted 30° to the symmetry axis) are different. Several studies have discussed this problem [e.g., *Dellinger and Vernik*, 1994; *Vernik and Liu*, 1997; *Dewhurst and Siggins*, 2006]

and concluded that with standard laboratory methods, phase velocities are not always measured. In case of the Kimmeridge shale under study, *Hornby* [1998] used full waveform finite difference method modeling to configure the experimental setup with the expected maximum range of elastic anisotropy and confirmed that the phase velocity was obtained for all off-axis measurements. Henceforth, when discussing elastic wave velocities, we will always mean phase velocities, unless specified otherwise.

[52] The values that *Hornby* [1998, Table 8] obtained at 80 MPa pressure, including his estimated uncertainties, are

$$^{exp}C_{ij} : C_{11} = 56.2 \pm 4.4; C_{13} = 20.5 \pm 2.3;$$
$$C_{33} = 36.4 \pm 2.3; C_{44} = 10.3 \pm 0.4;$$
$$C_{66} = 18.9 \pm 0.1 \text{ [GPa]}. \tag{15}$$

[53] *Hornby's* [1998] paper does not contain information about the shale density at 80 MPa. We used reported elastic coefficients and measured wave velocity values to find the best fit density value and determined it to be 2.648 g/cm³. Taking all the minerals with volume fractions listed in Table 1 and density values (see Table S1 in the supporting information), the resulting density of the sample without pores and cracks would be 2.854 g/cm³. If all density estimates are correct, then at 80 MPa pressure the shale sample should have ≈ 7.2% of empty or ≈ 11.1% of water-filled pores (assuming a zero density for empty and 1 g/cm³ density for water-filled pores). It is possible that mineral (especially phyllosilicate) densities that we consider could be overestimated or underestimated as they have been calculated or measured for "ideal" compositions. For example, density values for kaolinite and illite-mica listed by *Katahara* [1996] are lower than those in *Militzer et al.* [2011] that we use here. Our Figure 2 shows the presence of iron and variations of Al/Si ratio in phyllosilicates that

Table 4. Components of Stiffness Tensor [GPa] of Kimmeridge Shale Constituents Calculated Using Different Averaging Models and Maximum to Minimum Young's Moduli Ratio E_{max}/E_{min} for Single Crystals

Mineral	E_{max}/E_{min}	Model	C_{11}	C_{13}	C_{33}	C_{44}	C_{66}
Quartz	1.8	Voigt	101.4	6.2	$=C_{11}$	$=(C_{11}-C_{13})/2$	$=(C_{11}-C_{13})/2$
		Reuss	92.7	9.8	$=C_{11}$	$=(C_{11}-C_{13})/2$	$=(C_{11}-C_{13})/2$
		GEO	96.9	8.1	$=C_{11}$	$=(C_{11}-C_{13})/2$	$=(C_{11}-C_{13})/2$
Pyrite	1.5	Voigt	329.4	60.1	$=C_{11}$	$=(C_{11}-C_{13})/2$	$=(C_{11}-C_{13})/2$
		Reuss	319.6	65.0	$=C_{11}$	$=(C_{11}-C_{13})/2$	$=(C_{11}-C_{13})/2$
		GEO	324.3	62.7	$=C_{11}$	$=(C_{11}-C_{13})/2$	$=(C_{11}-C_{13})/2$
Albite	3.4	Voigt	118.5	36.2	$=C_{11}$	$=(C_{11}-C_{13})/2$	$=(C_{11}-C_{13})/2$
		Reuss	94.5	35.0	$=C_{11}$	$=(C_{11}-C_{13})/2$	$=(C_{11}-C_{13})/2$
		GEO	106.4	37.6	$=C_{11}$	$=(C_{11}-C_{13})/2$	$=(C_{11}-C_{13})/2$
Kaolinite	4.5	Voigt	142.9	32.5	100.7	37.8	47.2
		Reuss	97.9	33.2	77.4	22.7	31.2
		GEO	122.2	34.3	87.3	28.7	39.4
Illite-mica	3.4	Voigt	145.3	37.2	94.4	37.2	51.3
		Reuss	107.7	28.8	73.1	26.9	37.7
		GEO	129.6	35.2	82.8	30.9	44.6
Illite-smectite	11.0	Voigt	116.1	22.8	81.4	36.8	45.0
		Reuss	46.7	11.0	35.0	13.9	17.1
		GEO	81.4	18.4	53.1	22.7	30.0

were not considered by *Militzer et al.* [2011]. Thus, values of 7.2% and 11.1% could be in turn overestimated or underestimated. On the other hand, *Hornby* [1998] reported a density of 2.69 g/cm³ for the shale "matrix" which results at 80 MPa pressure in ≈1.6% "empty" pores or 2.5% of water-filled pores. *Hornby* [1998] estimated a porosity of 2.5% as measured by helium expansion. These values seem too low. Some problems of helium expansion porosimetry have been discussed by *Twardowski et al.* [2004]. They noted that discrepancies in sample porosity of up to 4% could be observed. It is also evident that it could not include isolated pores that are present in the shale sample (Figures 1 and 4). Our X-ray tomography data resulted in 6.3% volume fraction of low-density features at atmospheric pressure that is in between *Hornby's* [1998] measurements and estimates made from mineral volume fractions and densities. As we noted, X-ray tomography porosity estimates do not include grains and pores with dimension less than 1 μm, but at 80 MPa pressure, some of these pores, especially very thin ones, should be closed.

[54] As a result of these considerations, we conclude that the overall porosity of the sample is poorly constrained, and it had to be taken as a "fit" parameter (within reasonable boundaries, i.e., less than 12%) in order to explain $^{exp}C_{ij}$ or related experimental velocities. To be consistent, for all the calculations of elastic wave velocities in the Kimmeridge shale models, we will use the same density of 2.648 g/cm³, regardless of the actual density of the model.

4. Models for Calculating Elastic Properties of Kimmeridge Shale

[55] Next, microstructural information on Kimmeridge shale should be incorporated into averaging models described in section 2. This includes mineral volume fractions, densities, crystallographic, and shape preferred orientations of grains, as well as grain shapes. Also, the presence of pores of different shape has to be accounted for. We will consider different types of models to explore their applicability by comparison with *Hornby's* [1998] experimental results and

highlighting the influence of different parameters on bulk elastic properties.

4.1. Calculation of Bulk Elastic Properties Without Consideration of Shapes and Pores

[56] We start by reviewing simple averaging models with spherical {1:1:1} grains and without consideration of porosity.

[57] Single crystal elastic properties are averaged over orientation distributions *f(g)* for each phase, using a micromechanical model (Voigt, Reuss, geometric mean—GEO), and corresponding elastic tensor components for the aggregate are obtained: two for quartz, pyrite, and albite with random orientation distributions and five independent coefficients in the case of textured kaolinite, illite-mica, and illite-smectite (Table 4). The difference between results of micromechanical models, especially Voigt and Reuss averages, increases with increasing elastic anisotropy of single crystals, as expressed by the ratio of maximum and minimum Young's moduli.

[58] After calculating averages for individual phases, all the phase components have to be combined, using the same micromechanical model and corresponding volume fractions from Table 1. The five averaged coefficients $^{model}C_{ij}$ resulting

Table 5. Components of Stiffness Tensor C_{ij} [GPa] of Transversely Isotropic Kimmeridge Shale Calculated Using Different Averaging Models[a]

Model	C_{11}	C_{13}	C_{33}	C_{44}	C_{66}
Voigt	132.4	25.7	104.1	44.2	51.4
Reuss	75.2	17.3	58.7	23.0	28.2
GEO	107.0	23.1	80.2	32.8	40.6
GMS {1:1:1}	107.3	21.2	81.1	34.2	41.8
GMS {1:1:0.1}	97.5	19.4	74.7	31.4	37.9
GMS {1:1:0.05}	95.9	20.0	74.0	30.6	36.8
GMS {1:1:0.01}	94.1	20.8	73.2	29.6	35.4
GMS {1:1:0.001}	93.6	21.2	73.1	29.3	35.0
$^{exp}C_{ij}$ at 80 MPa	56.2	20.5	36.4	10.3	18.9

[a]*Hornby's* [1998] experimental values $^{exp}C_{ij}$ at 80 MPa are given for comparison. See text for model descriptions.

from application of Voigt, Reuss, and GEO models are given in Table 5, as well as results of the GMS algorithm for spherical grain shape (GMS {1:1:1}). As expected, values for a Voigt average are much higher than a Reuss average and the geometric mean is in between. We note the similarity between GEO and GMS {1:1:1} results. Elastic tensor coefficients for these two models differ by less than 2 GPa; the biggest difference is in the C_{13} coefficients ($\approx 8\%$, 1.9 GPa).

[59] Comparing GEO and GMS {1:1:1} results with experimental values, it is evident that $^{model}C_{11}$, $^{model}C_{33}$, and $^{model}C_{66}$ values should be reduced about 2 times, $^{model}C_{44}$ 3.5 times, and the $^{model}C_{13}$ value should be conserved.

4.2. Effects of Grain Shape on Bulk Elastic Properties

[60] Next we will improve the model by considering the platelet shape of phyllosilicate grains with the self-consistent algorithm GMS. As described in sections 3.6 and 3.7, we take into account the relationship between crystal and grain coordinate systems of phyllosilicates and perform the averaging using F(Ω). Quartz, pyrite, and albite grains are considered to be spheres. For simplicity, we assume that all phyllosilicate grains have the same aspect ratio ζ (written in coordinate system K_E: {X_E,Y_E,Z_E}), i.e., {1:1:ζ} for kaolinite and {ζ:1:1} for illite-mica and illite-smectite in first monoclinic setting. All the minerals are taken with their respective volume fractions and orientation distributions. The $^{model}C_{ij}$ are given in Table 5 where GMS {1:1:0.1} denotes the model with $\zeta = 0.1$, etc.

[61] As a result of grain shape consideration, all $^{model}C_{ij}$ values decrease, except for the $^{model}C_{13}$ value that does not change significantly. But it is remarkable that a decrease of ζ decreases $^{model}C_{33}$ as well as $^{model}C_{11}$, and it also decreases P wave anisotropy and maximal shear wave splitting. This is in contradiction, e.g., with calculations made for mica-bearing aggregates by *Nishizawa and Yoshino* [2001]. *Wenk et al.* [2012] also observed an increase in P wave anisotropy when the shape of biotite grains was taken into account. However, their calculations have only been made for low volume fractions of highly oriented mica ($< 30\%$) in an isotropic (or almost isotropic) matrix. In our case the volume fraction of phyllosilicates is 66.8% and ODFs have a large number of randomly oriented grains (f_{min} values in Table 2). We conclude that the effect of simultaneous decrease of $^{model}C_{11}$ and $^{model}C_{33}$ when decreasing ζ value in materials consisting of an isotropic matrix and anisotropic grains with shape {1:1:ζ} ($\zeta \le 1$) could develop at higher volume fractions of these anisotropic grains and/or when their texture index F_2 is low.

[62] Decreasing ζ below 0.1 does not have a pronounced impact on stiffness coefficients C_{ij}, an effect already noted by *Nishizawa and Yoshino* [2001]. Even assuming an ultrathin (and obviously unrealistic) grain shape with $\zeta = 0.001$, it is only possible to decrease $^{model}C_{11}$ and $^{model}C_{33}$ by 3.9 and 1.6 GPa, respectively, compared with $\zeta = 0.1$. Thus, we can assume that shale models where different phyllosilicate minerals have grain aspect ratios within a realistic range ($0.01 < \zeta < 0.1$, Figure 3a and 3c), and shale models where all the phyllosilicate grains have the same aspect ratio, will have similar $^{model}C_{ij}$ values. This infers that further modeling could be greatly simplified by assuming that all phyllosilicate grains have the same shape. From these simulations, it is also clear that mineral-preferred orientations and grain shapes alone cannot describe elastic properties of shale.

4.3. Effects of Different Types of Pores on Bulk Elastic Properties

[63] We will now investigate the possibility to describe $^{exp}C_{ij}$ by considering presence of different types of pores in the sample. It is known that thin platelet-shaped pores greatly influence bulk elastic properties of shales [e.g., *Sayers*, 2008]. Since the shale model is transversely isotropic, we assume that also the pore orientation distribution has fiber symmetry, with the fiber axis normal to the bedding plane, or has a random orientation distribution. Orientation distributions of pores are described in a macroscopic sample coordinate system with a SODF. In case when the shape of the pore is symmetric with respect to the bedding plane normal (spherical pores, or completely aligned low aspect ratio pores parallel to the bedding plane), it is possible to use for them the "single crystal"-like δ-function SODF (with only non-zero value at {α, β, γ} = {0°, 0°, 0°}) to speed up the self-consistent computation. Pores could either be "empty" (e.g., air) or filled with water or kerogen. We will test the following cases: (1) spherical pores; (2) platelet-shaped {1:1:ζ} ($\zeta < 1$) pores aligned parallel to the bedding plane; (3) platelet-shaped {1:1:ζ} ($\zeta < 1$) pores that are perpendicular to the bedding plane: their shortest direction is aligned in the bedding plane, and they effectively possess a fiber texture with fiber axis perpendicular to the bedding plane; (4) platelet-shaped {1:1:ζ} ($\zeta < 1$) pores with a random SODF; and combinations of several types of pores, as TEM and SEM observations (Figures 1–4) show that in the shale sample both high and low aspect ratio pores are present and low aspect ratio pores have more complex orientation distributions. Here we want to highlight the influence of specific types of pore systems and assume perfect alignment of pores relative to sample coordinates. We use a GMS {1:1:0.05} model (Table 5) as anisotropic matrix and add pores into it.

[64] We will investigate effects of both empty and water-filled pores up to 10% of total porosity. We assume that for empty pores all $C_{ij} = 0$; for the water we use the following stiffness coefficients: $C_{11} = C_{12} = C_{13} = C_{22} = C_{23} = C_{33} = 2.2$ GPa, and all others are zero [*Hornby et al.*, 1994; *Arns et al.*, 2002]. Introduction of these elastic constants does not necessarily mean that pores are indeed air filled or water filled. For example, stiffness coefficients of water correspond closely to those of 50 API oil at room temperature and ≈ 80 MPa pressure (≈ 2.3 GPa, as can be deduced from *Castagna et al.* [1993, Figure 17]). Microtomography does suggest presence of some kerogen (Figure 6b).

[65] A brief summary of the $^{model}C_{ij}$ values for material with different empty and water-filled pores is given in Table 6, and an expanded version is provided as Table S2 in the supporting information for empty and Table S3 for water-filled pores. It is clear that pores can only decrease elastic constants of an initial anisotropic medium. But different types of pores decrease each stiffness coefficient $^{model}C_{ij}$ differently.

[66] All $^{model}C_{ij}$ values drop almost linearly with increasing volume fraction of spherical pores (either empty or water filled); and an addition of 1 vol % of spherical pores decreases all $^{model}C_{ij}$ values by $\approx 2\%$. Also, $^{model}C_{ij}$ values are almost the same for material with the same amounts of spherical air or water-filled pores. In particular, $^{model}C_{44}$

Table 6. Components of Stiffness Tensor C_{ij} [GPa] of Transversely Isotropic Kimmeridge Shale Calculated Adding Different Volume Fractions of Empty or Water-Filled Pores of Different Shape to Model GMS {1:1:0.05} (Table 5)

Volume Percent, Type of Pores	Shape and Orientation of Pores	C_{11}	C_{13}	C_{33}	C_{44}	C_{66}
0.0		95.9	20.0	74.0	30.6	36.8
1.0, empty	{1:1:1}	93.9	19.6	72.5	30.0	36.0
	{1:1:0.1} ‖ to bedding plane	94.3	17.9	65.0	28.7	36.3
	{1:1:0.01} ‖ to bedding plane	91.2	6.0	21.5	19.8	36.4
	{1:1:0.1} ⊥ to bedding plane	88.4	18.4	72.7	29.4	34.3
	{1:1:0.01} ⊥ to bedding plane	42.1	8.1	69.3	22.7	18.7
	{1:1:0.1} random	90.2	18.3	69.9	29.2	34.9
	{1:1:0.01} random	39.2	2.7	33.2	16.3	18.2
1.0, water-filled	{1:1:1}	94.0	19.7	72.6	30.0	36.0
	{1:1:0.1} ‖ to bedding plane	94.5	18.6	67.4	28.7	36.3
	{1:1:0.01} ‖ to bedding plane	94.0	16.2	58.2	20.4	36.4
	{1:1:0.1} ⊥ to bedding plane	89.8	18.9	72.9	29.4	34.5
	{1:1:0.01} ⊥ to bedding plane	75.5	16.9	72.3	23.1	26.5
	{1:1:0.1} random	91.2	18.9	70.7	29.3	35.0
	{1:1:0.01} random	77.0	19.4	61.9	23.9	27.9
10.0, empty	{1:1:1}	76.4	16.1	59.6	24.6	29.2
	{1:1:0.1} ‖ to bedding plane	81.5	7.7	23.6	16.7	32.2
	{1:1:0.01} ‖ to bedding plane	80.5	0.3	0.7	2.4	32.6
	{1:1:0.1} ⊥ to bedding plane	41.5	9.2	62.4	19.8	17.0
	{1:1:0.01} ⊥ to bedding plane	0.4	0.2	59.6	1.9	0.2
	{1:1:0.1} random	49.7	8.2	40.3	17.7	20.3
	{1:1:0.01} random	-	-	-	-	-
10.0, water-filled	{1:1:1}	77.2	16.9	60.4	24.6	29.2
	{1:1:0.1} ‖ to bedding plane	82.9	11.4	34.6	17.1	32.2
	{1:1:0.01} ‖ to bedding plane	83.0	7.4	22.3	4.3	32.7
	{1:1:0.1} ⊥ to bedding plane	51.3	12.3	63.8	20.0	19.2
	{1:1:0.01} ⊥ to bedding plane	21.9	7.7	62.9	4.6	2.9
	{1:1:0.1} random	57.5	12.6	46.8	19.0	21.9
	{1:1:0.01} random	18.7	14.6	18.2	19.1	19.6

and $^{\text{model}}C_{66}$ are exactly the same. This is in agreement with calculations made for an isotropic medium with spherical pores by *Le Ravalec and Guéguen* [1996]. According to their data, there is an almost linear dependence of stiffness coefficients on porosity for porosities less than 20%. Thus, to reduce coefficients of the shale model by ≈ 40–50% (to be roughly comparable with $^{\text{exp}}C_{ij}$ values), about 20–25 vol % of spherical pores would have to be added. But porosity of this scale is far above experimental estimates.

[67] From Table 6, it is evident that adding {1:1:ζ} pores aligned parallel to the bedding plane to the model significantly decreases $^{\text{model}}C_{33}$. This decrease is more pronounced for low aspect ratio pores. Adding {1:1:ζ} pores aligned perpendicular to the bedding plane significantly decreases $^{\text{model}}C_{11}$ and $^{\text{model}}C_{66}$. Models with the same volume fraction of {1:1:ζ} pores aligned parallel and perpendicular to the bedding plane are characterized by similar $^{\text{model}}C_{13}$ and $^{\text{model}}C_{44}$ values.

[68] Randomly oriented {1:1:ζ} pores decrease all the $^{\text{model}}C_{ij}$ values, and this decrease is again more pronounced with decreasing aspect ratio ζ. Empty randomly oriented {1:1:0.01} pores practically "destroy" the sample when their volume reaches ≈ 2.5 vol %, with all $^{\text{model}}C_{ij}$ values converging to 0. One can imagine that accommodating a relatively high volume fraction of random low aspect ratio pores within self-consistent GMS algorithm means that statistically the material is crossed by propagating "cracks" in multiple directions, resulting in zero stiffness. Water-filled randomly oriented {1:1:ζ} pores demonstrate another peculiarity: decrease of aspect ratio ζ from 0.1 to 0.01 (for the same

porosity) leads to an increase of the $^{\text{model}}C_{13}$ coefficient. This effect is not observed for pores oriented parallel or perpendicular to the bedding plane. But in general, all types of pores under consideration decrease the C_{13} value of an initial anisotropic elastic matrix, and thus, every $^{\text{model}}C_{13}$ of material with pores is lower than the experimental $^{\text{exp}}C_{13}$ (equation (15)).

[69] It is obvious that just one single type of pore with a "simple" orientation distribution is not sufficient to describe all $^{\text{exp}}C_{ij}$ (Tables S2 and S3 in the supporting information). But it is possible to combine several types of pores, e.g., {1:1:ζ} aligned parallel and perpendicular to the bedding plane to decrease different $^{\text{model}}C_{ij}$ coefficients differently to match $^{\text{exp}}C_{ij}$. Several models that feature two or three types of pores are listed in Table S4 in the supporting information. Here we will only mention some of them, using the same model numbers (e.g., model #1) as in Table S4 in the supporting information.

[70] First, we should note that addition of empty low aspect ratio pores to the model reduces the $^{\text{model}}C_{44}$ coefficient much less compared to other coefficients. Low aspect ratio pores aligned parallel to the bedding plane reduce the $^{\text{model}}C_{33}$ value more strongly than the $^{\text{model}}C_{44}$ value (Tables 6 and S2 in the supporting information). Thus, the ratio $^{\text{model}}C_{33}/^{\text{model}}C_{44}$ in models containing such pores is much lower than the experimental value. Our calculations show that this feature also applies to models with several types of pores. For example, model #1 in Table S4 in the supporting information that contains 1 vol % of {1:1:0.01} empty pores aligned parallel to the bedding plane and 1 vol %

Table 7. Components of Stiffness Tensor C_{ij} [GPa] of Transversely Isotropic Kimmeridge Shale Calculated by Adding Low Aspect Ratio {1:1:0.01} Water-Filled Pores With Different Orientation Distributions (SODF) and Spherical {1:1:1} Water-Filled Pores to Model GMS {1:1:0.05} (Table 5)[a]

#	Volume Percent Pores {1:1:0.01}	SODF of Pores: Random Distribution (RO) + GFC	Volume Percent Pores {1:1:1}	C_{11}	C_{13}	C_{33}	C_{44}	C_{66}
1	3.5	0.3 RO + 0.7 GFC 35°	-	60.5	17.1	38.8	11.6	21.1
2	3.5	0.3 RO + 0.7 GFC 45°	-	57.5	17.8	38.6	12.0	19.6
3	3.5	0.35 RO + 0.65 GFC 35°	-	59.4	17.2	39.0	11.6	20.5
4	3.5	0.35 RO + 0.65 GFC 45°	-	56.7	17.9	38.8	12.0	19.1
5	4.0	0.35 RO + 0.65 GFC 45°	-	52.7	17.6	36.2	10.6	17.3
6	3.5	0.3 RO + 0.7 GFC 35°	1.0	59.0	16.9	38.0	11.3	20.5
7	3.5	0.3 RO + 0.7 GFC 35°	3.0	56.0	16.3	36.3	10.6	19.2
[exp]C_{ij} at 80 MPa				56.2	20.5	36.4	10.3	18.9

[a]*Hornby's* [1998] experimental values [exp]C_{ij} at 80 MPa are given for comparison. The Gauss fiber component (GFC) is described by full width at half maximum (FWHM). See text for model descriptions.

of {1:1:0.01} empty pores with orientation perpendicular to the bedding plane have the following coefficients:

$$^{model}C_{ij}: \quad C_{11} = 32.0; C_{13} = 2.4; C_{33} = 13.2;$$
$$C_{44} = 10.9; C_{66} = 14.8 \text{ [GPa]}. \quad (16)$$

[71] As we see, $^{model}C_{44}$ is of the right order, but values of all other elastic coefficients are too low. By considering different volume fractions and aspect ratios of pores, it is possible to get, e.g., $^{model}C_{11}$ and $^{model}C_{33}$ values close to corresponding $^{exp}C_{ij}$ (model #3 containing 2.5 vol % of {1:1:0.05} empty pores aligned parallel to the bedding plane and the same amount of same pores with orientation perpendicular to the bedding plane):

$$^{model}C_{ij}: \quad C_{11} = 60.8; C_{13} = 8.1; C_{33} = 37.4;$$
$$C_{44} = 18.7; C_{66} = 25.0 \text{ [GPa]}, \quad (17)$$

but in this case $^{model}C_{44}$ is unrealistically high, and $^{model}C_{13}$ remains well below the experimentally determined value (equation (15)).

[72] In general, we were unable to reach a good "balance" between different $^{model}C_{ij}$ coefficients in models containing empty pores (see Table S4 in the supporting information for examples). This is consistent with the assumption that probably empty pores are not present in the sample at 80 MPa (section 3.8). Thus, we will concentrate on water-filled pores in our following modeling of shale properties at this pressure.

[73] Contrary to empty pore models, for water-filled pores several combinations are possible that result in $^{model}C_{ij}$ values that are close to corresponding $^{exp}C_{ij}$. Stiffness coefficients of model #8 (Table S4 in the supporting information) that contains 6.5 vol % of {1:1:0.05} water-filled pores aligned parallel to the bedding plane and 3.5 vol % of {1:1:0.03} water-filled pores with orientation perpendicular to the bedding plane differ from experimental values (equation (15)) by less than 8% except for C_{13}:

$$^{model}C_{ij}: \quad C_{11} = 53.7; C_{13} = 8.6; C_{33} = 33.5;$$
$$C_{44} = 10.7; C_{66} = 18.9 \text{ [GPa]}. \quad (18)$$

[74] Apart from the low C_{13} value, this model introduces different aspect ratios for pores of different orientations, which is not supported by SEM and TEM observations (Figures 1

and 4). In model #10, with 2 vol % of water-filled pores aligned parallel and 2 vol % oriented perpendicular to the bedding plane, the same shape {1:1:0.01} is introduced to all pores independently of orientation. Elastic coefficients correspond closely to mean experimental values, despite a 2.5 times lower porosity than in case of model #8 (equation (18)).

[75] Models with combinations of random low aspect ratio pores and pores aligned parallel to the bedding plane provide even better numerical agreements between $^{model}C_{ij}$ and $^{exp}C_{ij}$. For model #11 (2 vol % of random water-filled pores and 2 vol % of water-filled pores aligned parallel to the bedding plane, pore aspect ratios are {1:1:0.01}), stiffness coefficients differ from experimental values by less than 5%, except for $^{model}C_{13}$ that is ≈24% lower than the experimental value:

$$^{model}C_{ij}: \quad C_{11} = 57.2; C_{13} = 15.5; C_{33} = 38.0;$$
$$C_{44} = 9.8; C_{66} = 19.2 \text{ [GPa]}. \quad (19)$$

[76] In model #11 (Table S4 in the supporting information), the volume of low aspect ratio pores could be slightly reduced and spherical water-filled pores could be added instead (to account for TEM/SEM observations of high aspect ratio pores in shale; Figures 1, 2, and 4), resulting in model #13:

$$^{model}C_{ij}: \quad C_{11} = 57.2; C_{13} = 15.4; C_{33} = 38.2;$$
$$C_{44} = 10.0; C_{66} = 19.3 \text{ [GPa]}. \quad (20)$$

[77] In this model 1.9 vol % of {1:1:0.01} pores are random and 1.9 vol % are parallel to the bedding plane. In addition there are 1 vol % of spherical pores, resulting in a total porosity of 4.8% and a density of 2.765 g/cm³. Stiffness coefficients are almost the same as in equation (19).

4.4. Consideration of General Fiber SODF for Flat Pores

[78] In the previous section, we have investigated the influence of shape, orientation, and volume fraction for ideally oriented pores. A reasonable agreement between $^{model}C_{ij}$ and $^{exp}C_{ij}$ can be obtained, especially with a combination of random and aligned pores. We will now advance to more realistic pore distributions.

[79] Aiming for better agreement with microstructural observations, we introduce a standard Gauss function component (GFC) defined by the full width at half maximum
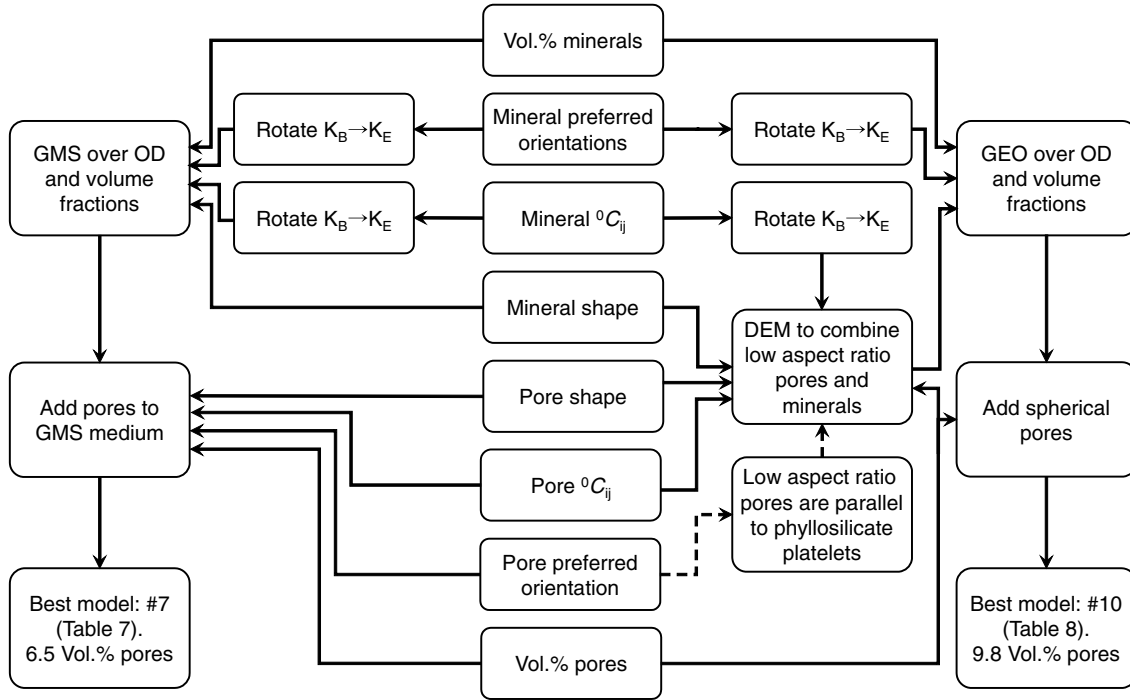
Figure 11. Sketch illustrating modeling procedures for self-consistent approach (left side) and differential effective medium approach (right side). Input parameters are in the center.

(FWHM) superposed on a fraction of randomly oriented pores (RO) to describe the SODF of flat pores. The fiber axis is parallel to the bedding plane normal and the shortest axis of the pore (Z_E). From section 4.3, it is evident that the vol % of low aspect ratio water-filled pores in the model should be close to 4. We varied pore contents near this value, the GFC/RO ratio, and the Gauss width in orientation space to explore the influence of these parameters on bulk elastic constants.

[80] Pores with aspect ratios {1:1:0.01} and model SODFs have been added to the anisotropic matrix (represented by the GMS {1:1:0.05} model, Table 5). Some examples are summarized in Table 7. It is evident that all models have elastic properties that are very close to $^{exp}C_{ij}$, except for $^{model}C_{13}$. The best agreement between model and experiment is reached for model #7, containing 3.5 vol % of low aspect ratio pores with a fiber SODF (0.3 RF and 0.7 GFC with 35° FWHM) and 3.0 vol % of pores with spherical shape. Differences between model and experimental elastic constants are within 0.3 GPa (< 3%), but for C_{13} it is 4.2 GPa (≈ 20%). Model #7 incorporates all available quantitative experimental information: single crystal elastic constants, ODFs, mineral volume fractions, and grain/pore shapes. The total porosity of 6.5% corresponds closely to tomography observations, and an RO component of 30% agrees with the randomly oriented part of phyllosilicates of 31.8%, based on Tables 1 and 2. A GFC FWHM of 35° means that distribution of shortest axes of low aspect ratio pores around the bedding plane normal has a width that is ≈ 10° less than the mean FWHM of the pole density distribution on main pole figures of phyllosilicates (and close to that of illite-mica, Table 2 and Figure 9).

[81] As a conclusion to this section on self-consistent modeling, we should again mention that all types of pore structures decrease $^{model}C_{13}$ values below the experimental value. This effect is least pronounced for low volume fractions of spherical pores (i.e., < 5%), but the addition of any volume fraction of low aspect ratio pores into the model results in a pronounced reduction of $^{model}C_{13}$.

[82] We summarize the self-consistent calculation process with a schematic sketch in Figure 11 (left side). The input data are volume fractions of pores and minerals, as well as their aspect ratios, orientation distributions, and stiffness coefficients. ODFs (and SODFs) are represented as 3-D numerical arrays with 5° resolution in orientation space. First, elastic constants and ODFs of phyllosilicates have to be rotated to change coordinate system from K_B to K_E. Next, an effective "pore-free" medium is created by averaging over ODFs and volume fractions of minerals with the GMS algorithm. Then pores are entered into this anisotropic medium. This produces a new set of elastic coefficients that describe the elastic properties of the porous shale. From these C_{ij}, elastic wave velocities can be calculated. Due to complexity of considered orientation distributions, the GMS refinement is time consuming. Even if a good starting suggestion of effective medium elastic constants is made, the algorithm (in a Fortran-based program) runs for several hours on a machine equipped with a third generation Intel Core i7 quad-core processor.

4.5. Models Using Differential Effective Medium (DEM) Approach

[83] Applying a self-consistent model GMS based on Eshelby's concept of ellipsoidal inclusions in a homogeneous matrix, it has been possible to obtain a fair agreement between model predictions constrained by microstructural observations and measured elastic properties of Kimmeridge shale. However, there are differences in the enigmatic
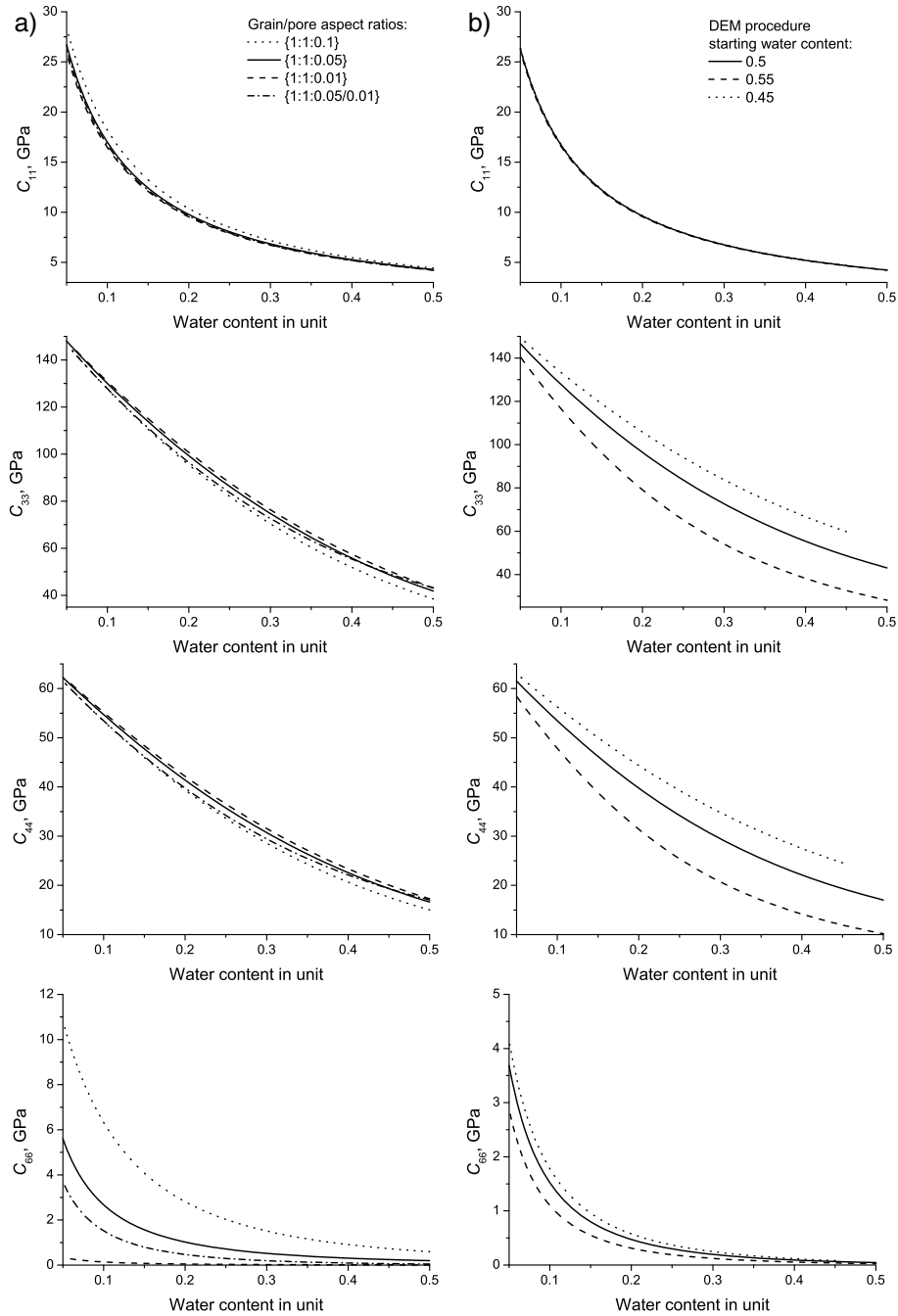
Figure 12. Dependence of some elastic constants of the DEM illite-mica/water unit on (a) water content and aspect ratio of grains and associated water-filled pores, and (b) different water content values at the start of DEM procedure.

coefficient C_{13}. Are these differences due to experimental errors, to uncertainties about single crystal elastic properties, or could they originate from limitations of the averaging model? We will explore this further by applying a differential effective medium (DEM) approach to modify single crystal elastic properties. This concept was introduced by *Bruggeman* [1935] to explain electrical conductivity in composite materials. The main idea is that properties of a multiphase material (effective medium) could be numerically calculated with a stepwise procedure, by incrementally adding inclusions of one phase into the host material, which is the homogeneous

effective medium obtained at the previous step. Such an approach has been applied to calculate properties of mineral aggregates, including sedimentary rocks and shales [e.g., *Nishizawa*, 1982; *Hornby et al.*, 1994; *Nishizawa and Kanagawa*, 2010; *Almqvist et al.*, 2011].

4.6. Mineral/Water DEM Units

[84] Here we follow the scheme proposed by *Hornby et al.* [1994] to model properties of shales and subsequently applied by, e.g., *Jakobsen et al.* [2000, 2001] and *Dræge et al.* [2006]. At a first step of this scheme, 0.5 of mineral

platelet-shaped grains and 0.5 of water-filled pores with corresponding aspect ratios are mixed with the self-consistent GMS algorithm to obtain properties of a new effective medium—a mineral/water DEM unit. Orientation distributions of both mineral grains and pores are considered to be δ-functions; i.e., mineral grains and pores are fully aligned and parallel to each other.

[85] At each subsequent step, new effective medium properties are calculated by combining the properties of the DEM unit obtained in the previous step (entered as anisotropic elastic matrix) and a small volume fraction of mineral, once again, with corresponding grain shape and δ-function ODF (with only nonzero value corresponding to $\{\alpha,\beta,\gamma\} = \{0°, 0°, 0°\}$). This procedure continues until the desired water content in the DEM unit is reached. This is performed for each of the three phyllosilicate minerals. The volume fraction of mineral added at each step ought to be infinitesimally small. We add ≈ 0.01 volume fraction of mineral at each step (in this case, 231 steps are required to reduce volume fraction of water in the DEM unit from 0.5 to 0.05).

[86] We assume that grains of all phyllosilicate phases have the same aspect ratio, and water-filled pores associated with grains of different phyllosilicates also have the same aspect ratio. Furthermore, we assume that all three mineral/water units have the same amount of water. The total water content—or total porosity—after each step can be easily calculated using mineral volume fractions in Table 1 and volume fraction of water in the DEM unit. For example, 0.05 of water in each DEM unit results in a sample porosity of ≈ 3.4 vol %, close to the low aspect ratio pores content in model #7 (Table 7). A 0.15 of water in DEM units results in a sample porosity of ≈ 10.5 vol % that is near upper limit of porosity estimates for the Kimmeridge shale sample (section 3.8).

[87] Figure 12a shows dependencies of some elastic coefficients (C_{11}, C_{33}, C_{44}, C_{66}) of the illite-mica/water DEM unit on water content and shape of grains and pores (note that C_{ij} are in monoclinic first setting with (100) as cleavage plane). $\{1:1:0.1\}$ denotes a model with both grains and low aspect ratio pores possessing the same shape. $\{1:1:0.05/0.01\}$ denotes the model where grains have shape $\{1:1:0.05\}$ and water-filled pores are five times thinner. The influence of aspect ratios within the water content range of interest (0.05–0.15) is most pronounced for the C_{66} coefficient of the DEM unit that in this case determines shear stiffness in the plane parallel to platelet-shaped grains and associated pores. If the aspect ratio of grain and corresponding pore is $\{1:1:0.01\}$, C_{66} is almost zero, even at water content of only 0.05. This DEM unit does not resist a shear in its basal plane. The C_{33} coefficient (one of the in-plane stiffnesses of the DEM unit) is also visibly affected by the aspect ratios with a difference between $\{1:1:0.1\}$ and $\{1:1:0.01\} \approx 4$ GPa at 0.15 water content in the unit, but due to a high absolute value of C_{33}, this difference is less than 4%. We note that the illite-mica/water DEM units with both grain and pore aspect ratios equal to $\{1:1:0.1\}$ have highest C_{11} (stiffness in direction perpendicular to platelets composing the DEM unit) and C_{66} coefficients among all considered units (Figure 12a). Units with grain and pore aspect ratios of $\{1:1:0.01\}$ are characterized by highest C_{33} and C_{44} coefficients.

[88] *Dræge et al.* [2006] suggested that the same aspect ratio could be used for all grains and pores in the DEM procedure. From Figure 12a, it is evident that in range of water contents of interest (0.05–0.15), absolute differences between $\{1:1:0.05\}$ and $\{1:1:0.05/0.01\}$ models are indeed small, but not negligible, and C_{44} and C_{33} are most influenced by the difference in aspect ratios. In section 4.7, we will investigate if this difference in DEM unit properties significantly affects bulk elastic properties of the shale obtained by orientation distribution and mineral volume fraction weighted averaging.

[89] As *Hornby et al.* [1994] stated, the DEM procedure that we use here has the ability to keep connectivity (percolation) of phases that were connected at the first step. Thus, in principle, the ratio of volume fractions of pores and mineral at the first step of the DEM can be different from 50:50 as long as the connection of phases is conserved. We investigated variants with 45:55 and 55:45 starting mineral/water volume ratios. Dependencies of coefficients C_{11}, C_{33}, C_{44}, C_{66} of the illite-mica/water DEM unit with a grain aspect ratio of $\{1:1:0.05\}$ and a pore aspect ratio of $\{1:1:0.01\}$ on starting water content of the DEM procedure are shown in Figure 12b. Apart from C_{11} that remains practically the same, the influence of water content at the start of the DEM procedure on elastic constants is considerable (Figure 12b) and in some cases even more pronounced than the influence of the grain and pore aspect ratios (Figure 12a). Generally, starting the DEM procedure at lower water content (e.g., 0.45 starting water content in the DEM unit, Figure 12b) results in higher stiffness coefficients of DEM units, though there are some exceptions, e.g., C_{13} of the kaolinite/water unit or C_{12} of the illite-smectite and illite-mica/water units are increasing with an increase of the starting water content.

[90] If the DEM unit construction starts at a water content close to 0.6, then resulting elastic coefficients at the first step converge to $C_{11} = C_{12} = C_{13} = C_{22} = C_{23} = C_{33} \approx 3.5$ GPa, and all others are equal to zero, independent of the mineral type and grain and pore aspect ratios (this holds for spherical pores as well as for low aspect ratio $\{1:1:0.01\}$ pores). It infers that the material is basically a liquid (a suspension) and mineral grains practically lost their percolation. This has been recognized for isotropic materials [e.g., *O'Connell and Budiansky*, 1974; *Berryman*, 1980a; *Jakobsen et al.*, 2001]. Thus, starting water content in the DEM procedure in the interval 0.4–0.6 should be considered when constructing DEM units. We recognize that the starting water content value is basically a model-dependent "fit" parameter that greatly influences elastic constants, as it is not constrained by any experimental data.

[91] Stiffness coefficients for DEM units with different water content are compared in Table 3 with single crystal coefficients. As expected, DEM units retain the symmetry of elastic properties of corresponding minerals, and with decreasing water content, elastic constants of units converge to elastic constants of corresponding single crystals. Absolute values of the DEM unit's stiffness coefficients are generally lower than corresponding coefficients of single crystals, though there are some interesting exceptions such as C_{13} of the DEM units of kaolinite and illite-smectite. For a starting water content of 0.5, grain shape $\{1:1:0.05\}$, and associated water-filled pore shape $\{1:1:0.01\}$, at water content of 0.05 and 0.127, C_{13} coefficients of these DEM units are higher than their single crystal counterparts (Table 3).

Table 8. Components of Stiffness Tensor C_{ij} [GPa] of Transversely Isotropic Kimmeridge Shale Calculated Using Different Averaging Models and DEM Units[a]

#	Water Content in DEM Unit	Volume Percent Pores in Model	Grain/Associated Pore Aspect Ratios	Averaging Method	C_{11}	C_{13}	C_{33}	C_{44}	C_{66}
1	0.050	3.4	{1:1:0.05}/{1:1:0.01}	GMS	81.5	19.0	53.2	21.3	30.4
2	0.127	8.8	{1:1:0.05}/{1:1:0.01}	Voigt	99.9	19.3	73.6	31.7	38.8
3	0.127	8.8	{1:1:0.05}/{1:1:0.01}	Reuss	21.4	13.0	17.5	2.7	4.1
4	0.127	8.8	{1:1:0.05}/{1:1:0.01}	GEO	59.5	20.8	35.7	10.5	18.6
5	0.127	8.8	{1:1:0.05}/{1:1:0.01}	GMS	64.4	15.5	38.2	15.4	23.6
6	0.127	8.8	{1:1:0.01}/{1:1:0.01}	GEO	49.7	25.2	30.6	4.9	11.6
7	0.127	8.8	{1:1:0.01}/{1:1:0.01}	GMS	62.8	15.9	36.6	14.2	22.6
8	0.127	8.8	{1:1:0.05}/{1:1:0.05}	GEO	63.8	19.4	38.2	12.9	21.3
9	0.127	8.8	{1:1:0.05}/{1:1:0.05}	GMS	67.0	15.2	39.9	16.7	24.9
10[b]	0.127	9.8	{1:1:0.05}/{1:1:0.01}	GEO	58.2	20.3	35.0	10.3	18.2
$^{exp}C_{ij}$ at 80 MPa					56.2	20.5	36.4	10.3	18.9

[a]DEM procedure starts at 50% water content in unit. *Hornby's* [1998] experimental values $^{exp}C_{ij}$ at 80 MPa are given for comparison. See text for model descriptions.
[b]This model is obtained by adding 1% of spherical water-filled pores to model #4.

4.7. Averaging DEM Units Properties Over ODF and Phase Volume Fractions

[92] Resulting mineral/water DEM units contain all shape and stochastic mixing related properties and could be considered as spherical "single crystals." Their orientation distribution in the sample coordinate system is described by SODFs F(Ω) of corresponding phyllosilicate minerals. In principle, the simple averaging schemes that we used in section 4.1 (e.g., Voigt, Reuss, and GEO) could be applied to calculate bulk elastic properties of the shale using DEM unit properties. SODFs have to be used instead of ODFs, since elastic properties of the DEM units are calculated in the grain coordinate system K_E. Other minerals with random orientation distributions—quartz, pyrite, albite, as well as spherical pores—can be added. *Hornby et al.* [1994] used an upper bound Hill and *Drœge et al.* [2006] a Voigt average over orientation distributions in their models. But since DEM units are extremely anisotropic (cf. Table 3), it means that Voigt-Reuss bounds and Hill approximations for textured aggregates containing these DEM units are very different.

[93] Results of application of different averaging models to Kimmeridge shale containing mineral/water DEM units are given in Table 8.

[94] We note that models described in Tables 6 and 7 reach acceptable agreement between $^{model}C_{ij}$ and $^{exp}C_{ij}$ when volume fractions of low aspect ratio pores in the model are 3.5–4%. When a DEM procedure is involved and GMS averaging is applied to DEM units, a model containing in total ≈3.4 vol % of water (water content in unit is 0.05) in low aspect ratio pores, associated with phyllosilicate platelets, demonstrates very high $^{model}C_{ij}$ values (model #1 in Table 8). Thus, compared to shale models with pores created using only GMS (equations (18) and (19) and all the models in Table 7), porosity in models involving DEM procedures should be higher, and we use DEM units with ≈0.127 water content (Table 3). The difference between Voigt and Reuss models is indeed very large (models #2 and #3 in Table 8). In section 4.1 we noted a similarity between elastic constants of shale models obtained by GEO and GMS algorithms, but when extremely anisotropic DEM units are considered, also GEO and GMS provide very different results (e.g., models #4 and #5 in Table 8). This difference mainly results from SODF-weighted averaging.

[95] The influence of phyllosilicate grain shapes on bulk elastic properties in the porosity range of interest (0.05–0.15 water content in DEM unit) is evident from a comparison of models #4 and #6, and also models #5 and #7 in Table 8. Differences between elastic constants of models with grain shapes of {1:1:0.05} and {1:1:0.01} are minimal (less than 2 GPa) when GMS averaging is applied, but they increase greatly in case of GEO averaging. Differences of the same scale are observed for different pore aspect ratios (cf. models #4 and #8, and also #5 and #9 in Table 8). Thus, using the same aspect ratio for grains and pores for DEM modeling as *Drœge et al.* [2006] suggested is not well justified, as results may be different, depending on the applied averaging method. Definitely, assuming different aspect ratios for grains and pores can improve the agreement between $^{model}C_{ij}$ and $^{exp}C_{ij}$.

[96] Comparison of different DEM shale models (some of them are given in Table 8) with $^{exp}C_{ij}$ (equation (15)) shows that if GMS averaging over SODFs (and volume fractions) is involved, then it is impossible to reach a good match between $^{model}C_{ij}$ and $^{exp}C_{ij}$. If $^{model}C_{11}$, $^{model}C_{33}$, and $^{model}C_{66}$ are estimated more or less correctly (e.g., model #7 in Table 8), then $^{model}C_{44}$ is usually 30–50% higher and $^{model}C_{13}$ is 20–40% lower than corresponding $^{exp}C_{44}$ and $^{exp}C_{13}$. If we adjust the starting water content of the DEM procedure (e.g., 42.5:57.5 mineral/water ratio at first DEM step), it is possible to reduce the difference between $^{model}C_{44}$ and $^{exp}C_{44}$ to ≈2 GPa (that is still ≈20%), but $^{model}C_{13}$ remains far below the experimental value.

[97] In contrast, if GEO averaging over SODFs and volume fractions is applied, it is possible to reach excellent agreement for all $^{model}C_{ij}$ and $^{exp}C_{ij}$ values (model #4 in Table 8). A 1 vol % of spherical water-filled pores could be added to this model for even better agreement with $^{exp}C_{ij}$ values and with TEM/SEM observations of high aspect ratio pores, resulting in model #10 in Table 8. This model has a total porosity of 9.8% and consequently a density of 2.673 g/cm³ that is close to our estimations made from *Hornby's* [1998] data (see section 3.8). Stiffness coefficients of this model differ from $^{exp}C_{ij}$ by less than 4%, and it appears to be the best solution. But is GEO averaging applicable in case of extremely anisotropic shale constituents?

[98] Before discussing related issues, we summarize the DEM procedure in the sketch of Figure 11 (right side). The
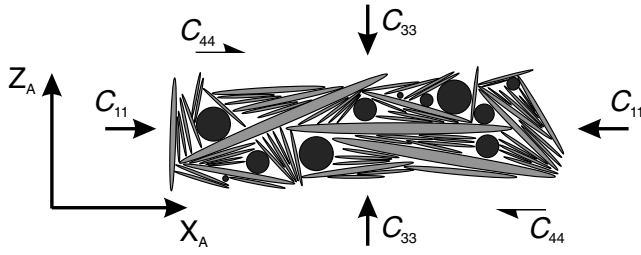
Figure 13. Sketch of the shale microstructure with ellipses representing phyllosilicates and black spheres components such as pyrite, quartz, and feldspar. Bedding plane is horizontal. Some C_{ij} coefficients of shale with arrows are indicated to illustrate their significance.

same microstructural input parameters (shapes of grains and pores, crystal preferred orientations) are used for DEM as for the self-consistent model. However, for DEM a first step is, after the consideration of coordinate systems (change K_B to K_E, sections 3.6 and 3.7), to create DEM mineral/water units. After an initial 50:50 mixture, mineral is added incrementally into an effective medium. With this procedure, we obtain modified "single crystal"-like elastic properties for phyllosilicates that include certain volume fractions of low aspect ratio pores and information on grain and pore shapes. Elastic properties of all components (DEM units and other minerals) are averaged over volume fractions and SODFs with the simple GEO algorithm, providing a geometric mean. Finally, a small percentage of high aspect ratio (spherical) pores is added into model for "perfect" agreement with experimental data.

5. Discussion

5.1. Summary of Results and Uncertainties About Input Parameters

[99] A set of complex experiments—SEM, TEM, X-ray diffraction, and microtomography—has been performed to study texture and microstructure of a Kimmeridge shale sample. Shapes of grains and pores, as well as mineral ODFs and volume fraction, have been measured and quantified. Microstructural characteristics of shale have been summarized by *Hornby et al.* [1994, Figure 7] in a schematic sketch of shale microstructure which was adapted by several researchers since then [e.g., *Bayuk et al.*, 2007; *Wenk et al.*, 2008; *Moyano et al.*, 2012]. A modified picture with a

significant volume fraction of phyllosilicates oriented with their least stiff direction close to bedding plane normal (Z_A axis) is shown in Figure 13. Low aspect ratio pores are mostly parallel to phyllosilicate grains which defines the $C_{33} < C_{11}$ relationship and low C_{44} (resistance to shear in bedding plane) value. As there are some platelet-shaped phyllosilicate grains oriented perpendicular to bedding plane of shale, the C_{44} value is higher than could be expected from the *Hornby et al.* [1994] model. The C_{13} coefficient controlling in-plane Poisson's expansion when the shale is subjected to compression along Z_A should have a relatively low value. Quartz and illite-smectite aggregates (55 vol % of sample, Table 1) have C_{13} below 20 GPa (Table 4). Also, an applied uniaxial compressive stress in Z_A should be accommodated to some degree by low aspect ratio pores in shale, thus reducing Poisson's expansion in the perpendicular direction. This microstructure provides the basis for our models. For convenience, we combine most important sets of elastic constants in Table 9.

[100] As expected, commonly used simple Voigt, Reuss, and GEO averages over mineral orientation distributions and phase volume fractions are not able to explain elastic properties of shale, composed of highly anisotropic phyllosilicates and low aspect ratio pores. This is also true for models that consider only spherical pores. Phyllosilicate grain shapes and low aspect ratio pores need to be included into models of bulk elastic properties of shales. We have shown that it is possible to use a modified self-consistent algorithm GeoMIXself (GMS) to produce an effective medium, consisting of all constituent minerals, with their corresponding phase volume fractions, orientation distributions, and mean grain shapes. Utilizing this effective medium as anisotropic matrix, we added with the GMS algorithm spherical and low aspect ratio water-filled pores with a fiber orientation distribution that is close to the measured ODFs of phyllosilicates (Figure 11, left side). As a result, we obtained model #7 in Table 7 (denoted as C in Table 9) that closely corresponds to experimental elastic constants $^{exp}C_{ij}$ at 80 MPa (A in Table 9) except for $^{model}C_{13}$ that is $\approx 20\%$ too low. The total porosity of this model is 6.5%.

[101] Aiming to improve this model, we utilized the DEM procedure to construct mineral/water units. In contrast with the previous model, where a self-consistent algorithm puts platelet-shaped pores with certain orientations into an effective medium (a mixture of all minerals in the sample with appropriate orientations and grain shapes) to calculate a new effective medium (and does not consider correlations in

Table 9. Summary of Most Important Experimental and Model Stiffness Coefficients of Kimmeridge Shale C_{ij} [GPa]

#	C_{11}	C_{13}	C_{33}	C_{44}	C_{66}	Remarks
A	56.2	20.5	36.4	10.3	18.9	$^{exp}C_{ij}$ at 80 MPa [*Hornby*, 1998]
B	57.6	11.7	37.8	10.8	19.2	$^{exp}C_{ij}$ at 80 MPa, based on 5 velocity measurements (section 5.4)
C	56.0	16.3	36.3	10.6	19.2	#7 (Table 7), GMS, 6.5 vol % pores
D	58.2	20.3	35.0	10.3	18.2	#10 (Table 8), DEM, 9.8 vol % pores
E	96.9	21.5	74.8	30.3	36.6	No pores, modified illite-smectite elastic tensor (section 5.3)
F	95.9	20.0	74.0	30.6	36.8	No pores, GMS {1:1:0.05} (Table 5)
G	48.4	16.4	27.3	7.8	17.0	$^{exp}C_{ij}$ at 5 MPa [*Hornby*, 1998]
H	49.4	12.6	27.9	7.7	17.5	$^{exp}C_{ij}$ at 5 MPa, based on 5 velocity measurements (section 5.4)
I	46.5	15.7	30.5	7.7	15.0	7.8 vol % pores, GMS (section 5.5)
J	46.3	12.9	27.6	8.3	16.0	7.3 vol % pores (including 0.1 vol % empty pores), GMS (section 5.5)
K	49.1	18.6	28.8	7.7	14.5	13.7 vol % pores, DEM (section 5.5)
L	49.3	15.4	26.0	8.5	15.9	11.6 vol % pores (including 0.1 vol % empty pores), DEM (section 5.5)

orientations of neighboring grains or pores), DEM relates pores to phyllosilicate platelets. The DEM procedure modifies single crystal elastic constants of phyllosilicates, taking into account shape and volume fractions of associated pores (Figure 11, right side). Using these DEM mineral/water units in place of separate phyllosilicates and low aspect ratio pores, we were able to achieve an excellent match of all $^{model}C_{ij}$ to $^{exp}C_{ij}$ by averaging DEM units over orientation distributions and phase volume fractions with the simple GEO (model #10 in Table 8 and D in Table 9, with a porosity of 9.8%). Though this model is numerically closer to experimental values of elastic coefficients than model C (Table 9), it involves GEO averaging over SODFs that is physically less well grounded. Also, the stepwise DEM procedure by itself is not straightforward as the direct application of a self-consistent scheme (e.g., GMS) depends on the initial water content in DEM units.

[102] Our two "best" models (C and D in Table 9) are close to experimental elastic constants (A in Table 9). They feature the same microstructural characteristics except for volume fractions of pores that are not well constrained by the experimental results we have. A number of simplifications had to be made to describe elastic properties of this complex multiphase material within the framework of available methods. We will briefly review these and highlight the points that need additional experimental investigation or necessary methodological improvements to reach a more refined description of shale properties.

5.2. Uncertainty of Porosity and Aspect Ratio Distributions

[103] The total porosity is an uncertainty, both at ambient conditions and at 80 MPa pressure (section 3.8), and our best suggestion was that at 80 MPa pressure, sample porosity is likely less than $\approx 12\%$. Both models are within this range. Model C (Table 9) has a lower porosity that is closer to the X-ray microtomography estimate; model D has higher porosity and a density that is closer to *Hornby's* [1998] estimate. Another issue is the distribution of pores on aspect ratios. Even though we considered only two kinds of pores (low aspect ratio pores of single shape {1:1:ζ} and spherical pores) in our modeling, we had to adjust their volume fraction fairly arbitrarily to get a better fit. In model C, the ratio of low aspect ratio pores volume to spherical pores volume is 3.5:3, and in model D, it is much higher: 8.8:1. Using only two types of pores {1:1:ζ} and {1:1:1} is a simplification, since there is a distribution of pore shapes in real material (Figure 3). The same is true for phyllosilicates that we have approximated by a single shape. We have shown that the dependence of $^{model}C_{ij}$ of model C (Table 9) on grain aspect ratios is minimal within the observed range of phyllosilicate grain aspect ratios ($0.01 < \zeta < 0.1$, section 4.2). In case of model D utilizing DEM units and GEO averaging over orientation distributions, the influence of grain shapes on resulting bulk elastic constants is more pronounced.

[104] The influence of aspect ratio distributions of pores on elastic properties of clay-water mixtures has recently been addressed by *Spikes* [2011] and *Moyano et al.* [2012], but only considering isotropic constituents. In our modeling, we take into account anisotropic single crystal elastic properties of minerals and average them over complex orientation distributions.

[105] As we noted (section 4.3), low volume fractions of spherical pores decrease all $^{model}C_{ij}$ coefficients almost linearly; an addition of 1 vol % of spherical pores decreases all $^{model}C_{ij}$ values by $\approx 2\%$. For low aspect ratio pores with simple orientations, the influence of different aspect ratios on bulk elastic properties is significant, as shown in Tables 6 and S2–S4 in the supporting information. When the DEM algorithm is used to relate phyllosilicate grains with low aspect ratio water-filled pores, the influence of shape of pores on properties of DEM units is not so pronounced (cf. models {1:1:0.05} and {1:1:0.05/0.01} on Figure 12a), and elastic coefficients responsible for in-plane shear stiffness of DEM units are most affected by the change of pore thickness, similar to results of *Moyano et al.* [2012]. But as we pointed out—after the orientation distribution and phase volume fraction averaging of elastic constants is performed—a 5 times decrease of pore thickness results in relatively small changes of elastic constants (cf. models #4 and #8 in Table 8). Thus, models involving DEM (Table 8) seem to be more stable with respect to changes in pore aspect ratios and consequently to pore aspect ratio distributions. But in general, determination and consideration of total sample porosity and volume distribution of grain and pore aspect ratios are extremely important for quantitative modeling of bulk elastic properties of shales.

5.3. Uncertainties Related to Single Crystal Properties

[106] Another source for errors of $^{model}C_{ij}$ values are uncertainties in single crystal elastic constants. It should be noted that even for well-known quartz, different high-quality measurements provide elastic constants that differ by ≈ 1 GPa [e.g., *Heyliger et al.*, 2003 versus *Ohno et al.*, 2006]. For some phyllosilicates, e.g., kaolinite, only ab initio estimates exist and results by *Sato et al.* [2005], *Militzer et al.* [2011], and *Karmous* [2011] differ significantly: C_{11} coefficients are 178.5, 169.1, and 209.0 GPa; C_{33} coefficients are 32.1, 81.1, and 68.5 GPa; and C_{13} coefficients are 2.0, 15.4, and 16.8 GPa correspondingly (all in K_B coordinate system). For illite-smectite, there are additional uncertainties, as water could be present in the illite-smectite structure between tetrahedral/octahedral sheets. Molecular dynamics simulations of complex montmorillonite structures related to illite-smectite indicate that elastic properties vary greatly with addition of water interlayers [e.g., *Suter et al.*, 2007; *Mazo et al.*, 2008a, 2008b].

[107] When averaging over measured orientation distributions is performed, one "wrong" single crystal coefficient can affect most of the bulk elastic constants. For example, if we arbitrarily increase C_{12} and C_{13} values of the illite-smectite single crystal (Tabel 3, "Dry") by a factor of 2, and use GMS to make a model without pores and with all phyllosilicate grains of the same shape {1:1:0.05}, we get elastic coefficients of model E (Table 9). Comparing them with the analogous GMS {1:1:0.05} model (F, Table 9) and other similar models from Table 5, it is clear that the effect of our arbitrary adjustment of those single crystal elastic constants on bulk elastic properties of shale is comparable with the effects caused by consideration of different grain shapes. Compositional and structural variations of phyllosilicates may introduce additional uncertainties into single crystal elastic constants.

[108] If modeling of material properties at increased pressure is performed, then pressure dependencies of single crystal elastic constants on pressure should be taken into account. At a relatively low pressure of 80 MPa, changes of elastic constants of quartz and pyrite are negligible. This is likely also the case for phyllosilicates. Elastic properties of some pore-filling fluids, on the other hand, may change significantly [e.g., *Hayward*, 1967; *Castagna et al.*, 1993].

5.4. Relationship of Measured Elastic Wave Velocities and Derived Stiffness Coefficients

[109] The only significant numeric difference between models C and D (Table 9) is in the C_{13} coefficient. But do existing experimental data (i.e., elastic wave velocities) provide good constrains?

[110] As was discussed by *Hornby* [1998], $^{exp}C_{ij}$ values are subject to experimental errors. In section 3.8, we briefly mentioned the phase/group velocity issue that should be resolved in interpretation of ultrasonic measurements, especially when attempting to solve bulk elastic tensor from velocity data. There are other complications. If Christoffel equations are used to estimate elastic constants from (phase) elastic wave velocities, their relationships with C_{ij} are

$$V_{PV} = \sqrt{\frac{C_{33}}{\rho}}, \qquad (21)$$

$$V_{SV1} = V_{SV2} = V_{SV} = \sqrt{\frac{C_{44}}{\rho}}, \qquad (22)$$

$$V_{PH} = \sqrt{\frac{C_{11}}{\rho}}, \qquad (23)$$

$$V_{SH} = \sqrt{\frac{C_{66}}{\rho}}, \qquad (24)$$

$$V_{SH30} = \sqrt{\frac{3C_{44} + C_{66}}{4\rho}}, \qquad (25)$$

$$V_{qP30} = \sqrt{\frac{C_{11} + 3C_{33} + 4C_{44} + \sqrt{A}}{8\rho}}, \qquad (26)$$

$$V_{qSV30} = \sqrt{\frac{C_{11} + 3C_{33} + 4C_{44} - \sqrt{A}}{8\rho}}, \qquad (27)$$

where

$$A = C_{11}^2 + 12C_{13}^2 + 9C_{33}^2 + 16C_{44}^2 + 4C_{11}C_{44} + 24C_{13}C_{44} \\ - 6C_{11}C_{33} - 12C_{33}C_{44} \qquad (28)$$

where ρ is density; V_{PV}, V_{SV1}, and V_{SV2} are wave velocities perpendicular to the bedding plane (one pure longitudinal wave PV and two pure shear waves, SV1 and SV2); V_{PH}, V_{SH}, and V_{SV} are wave velocities in the bedding plane (one pure longitudinal PH and two pure shear waves: SH with polarization parallel to the bedding plane, SV with perpendicular polarization); and V_{qP30}, V_{SH30}, and V_{qSV30} are velocities of waves propagating in a direction inclined by 30° to the bedding plane normal (one quasi-longitudinal qP30, pure shear SH30, and quasi-shear qSV30 waves; SH30 is polarized parallel to the bedding plane) [*Hornby*, 1998]. All the

nine measured velocity values are listed in *Hornby* [1998, Table 5].

[111] Though nine velocity measurements (three compressional and six shear wave velocities) were made on three cylindrical samples, both shear wave velocities in the direction parallel to the symmetry axis (V_{SV1} and V_{SV2}) and a slow shear wave velocity in the direction perpendicular to the symmetry axis (V_{SV}) should be equal (equation 22) but their measured values differ by more than 5%. The C_{13} coefficient only enters equations (26) and (27) for the quasi-longitudinal and quasi-shear velocities measured in the inclined direction (30° with the symmetry axis) and only together with C_{11}, C_{33}, and C_{44}, which makes it harder to determine C_{13} with high precision. The C_{66} coefficient also enters only two equations, one of them together with C_{44} that could be the cause for underestimating the experimental error (only 0.1 GPa according to *Hornby* [1998]).

[112] *Hornby* [1998] calculated the five stiffness coefficients by combining all nine velocity measurements and determining statistical errors (equation (15)). In B (Table 9), we show $^{exp}C_{ij}$ calculated based on equations (21)–(24) and (26) using only five velocity values: V_{PV}, V_{SV1}, V_{PH}, V_{SH}, and V_{qP30}. Most coefficients are very similar, except C_{13} which is much lower than in A and even below model C (Table 9). It indicates considerable uncertainty in $^{exp}C_{13}$, well beyond the estimated statistical error. $^{exp}C_{13}$ is the least constrained coefficient (by the experimental setup used), as was already suggested by *Hornby* [1998, Table 9]. In addition, since C_{13} only appears in equations in oblique directions, it is the only one subjected to the phase/group velocity issue [e.g., *Jakobsen and Johansen*, 2000; *Dewhurst and Siggins*, 2006]. It means that the difference in $^{model}C_{13}$ between experimental estimates A (or B) and models C and D (Table 9) cannot be used as a reliable indicator for validity or incorrectness of a model. We consider that both models C and D in fact give numerically "correct" elastic coefficients within experimental uncertainties.

[113] In Figure 14, we show experimentally measured elastic wave velocities in Kimmeridge shale at 80 MPa [*Hornby*, 1998] (squares), phase and group velocities recalculated from *Hornby*'s [1998] elastic constants $^{exp}C_{ij}$ (A in Table 9) and phase and group velocities of model C. This model better describes the measured *P* wave velocity in the off-axial direction; thus, it fails to describe (with acceptable precision) only one experimental point out of nine, compared to $^{exp}C_{ij}$ constants.

[114] It should be noted that the group velocity vector direction in an anisotropic material is generally different from the wave front normal (propagation direction), and thus, plotting group velocity versus propagation direction [e.g., *Dewhurst and Siggins*, 2006, Figure 5] does not reflect actual peculiarities of the wave propagation process. In Figure 14, the group velocity values are plotted versus group velocity vector direction. It is evident that elastic wave velocity measurements in multiple directions, for example, on spherical samples [e.g., *Vilhelm et al.*, 2010; *Lokajicek et al.*, 2011; *Bóna et al.*, 2012], could provide an overdetermined system of equations of type (equation (21)–(27)) to calculate bulk elastic constants with better statistical precision (and avoiding data points that could be subject to systematic errors). Such measurements could also reveal possible deviations from transverse isotropy [e.g., *Nishizawa and Kanagawa*, 2010] or inclination of the real symmetry axis
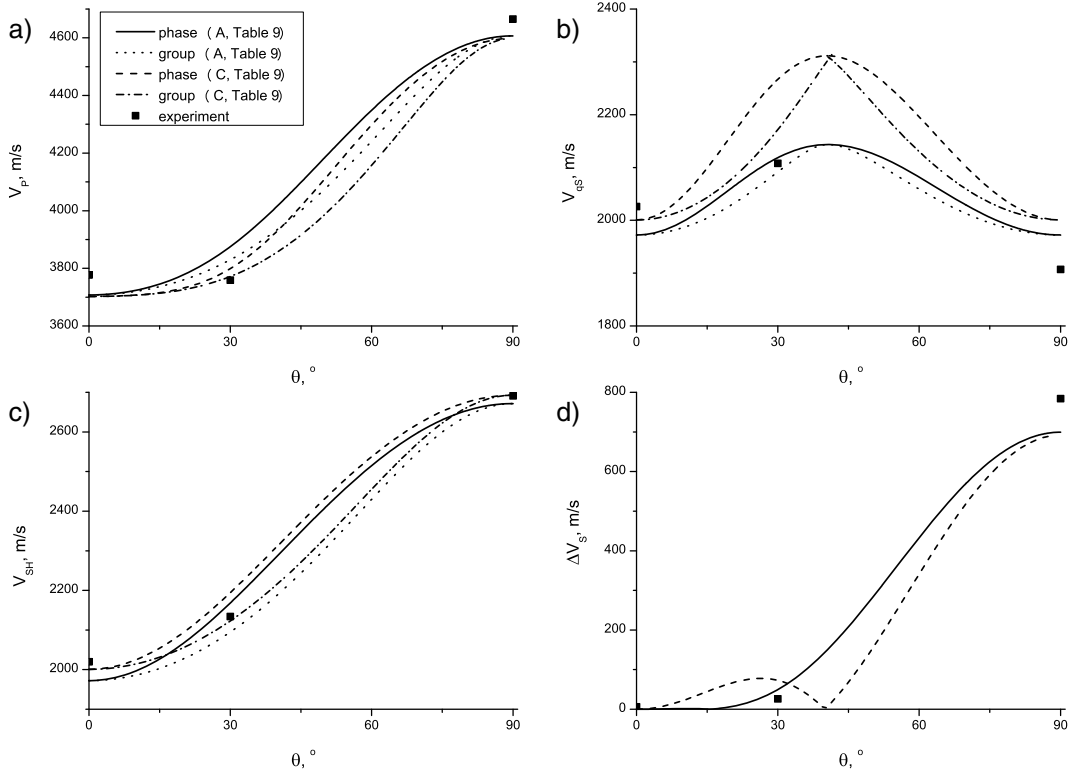
Figure 14. Velocities of (a) quasi-longitudinal, (b) quasi-shear, and (c) shear elastic waves in Kimmeridge shale at 80 MPa (experiment and calculation based on elastic constants estimations $^{exp}C_{ij}$ [*Hornby*, 1998], A in Table 9) and shale model (C, Table 9). (d) Shear wave splitting (phase velocities) is also shown. θ is the angle between bedding plane normal and propagation direction (for phase velocities) or group velocity vector direction (for group velocities).

of shale to the assumed macroscopic coordinate axis Z$_A$ [e. g., *Nadri et al.*, 2012].

5.5. Elastic Constants of Shale at Different Pressures

[115] Of great practical importance is the question whether our models can describe elastic constants of shale at different pressure by varying a minimal number of parameters. It is clear that aspect ratio distributions of pores and total porosity are most sensitive to pressure changes. According to the classical analysis of *Walsh* [1965], in isotropic media thin pores close first; the pressure needed to close spherical pores is comparable to Young's modulus of the material. In anisotropic materials the dependence of pore closure on pressure could be more complex, and it is reasonable to assume that as thinnest pores close, pores with lower aspect ratios become thinner. A similar pressure behavior was observed in porous reactor graphite [*Matthies*, 2012, Table 3]. Thus, we will only increase the volume fraction of low aspect ratio pores in our best models (C and D) to describe elastic properties at 5 MPa pressure (G, Table 9 from *Hornby* [1998, Table 8]), without changing their orientations, as well as volume fraction of spherical pores.

[116] If in model C the fraction of low aspect ratio water-filled pores is increased from 3.5 to 4.8 vol % (increase in total porosity to 7.8%), resulting stiffness coefficients (I, Table 9) are convincingly close to experimental values (G), with a correct C_{13} coefficient, but higher C_{33} and lower

C_{66} values (difference of ≈ 12%). It is conceivable that also empty low aspect ratio pores are opened at low pressure. Increasing in model C, the fraction of low aspect ratio water-filled pores to 4.2 vol % and also adding 0.1 vol % of empty pores yields model J (Table 9). Differences between G and J are within 2.1 GPa (< 6.4%) for all elastic constants except C_{13} that in model J is 21% lower: similar to the difference between model C and $^{exp}C_{ij}$ at 80 MPa pressure (A, Table 9). We also calculated $^{exp}C_{ij}$ from five velocity measurements analogous to B in Table 9 (see section 5.4). A comparison of these data (H, Table 9) with model J is even more favorable. We conclude that models of the type shown in Table 7 can describe elastic constants of Kimmeridge shale at pressures from 5 to 80 MPa with similar quality by considering changes in total sample porosity of ~ 1 vol %.

[117] In model D the water content in DEM units was increased from 0.127 to 0.18 to account for lower pressure (model K in Table 9). Differences between experimental values G and model K are less than 2.5 GPa. The total porosity of model K is 13.7 vol %, considerably above X-ray microtomography estimates. In this case we also can assume that some empty pores are opened, adjust the water content in DEM units to 0.15, and add 0.0015 of {1:1:0.01} empty pores into DEM units. Applying GEO averaging over orientation distributions and phase volume fraction results in $^{model}C_{ij}$ values L (Table 9) that differ from experimental

values by less than 1.3 GPa ($< 9\%$). The total porosity in this case is 11.6% (including $\approx 0.1\%$ of empty pores).

[118] Thus, with our assumption—more low aspect ratio pores are opened at lower pressures, including a very low fraction of empty pores (≈ 0.1 vol % at 5 MPa pressure)—we can describe elastic properties of shale with models of both types: utilizing only GMS or the DEM combined with GEO algorithms. Models with DEM units have considerably higher porosity and predict higher changes of porosity with pressure increase.

5.6.   Additional Remarks on Microstructure of Shale and Elastic Properties Averaging

[119] Considering models D and L (Table 9), we should note that GEO averaging over ODFs is a statistical/mathematical procedure, though it satisfies the important "inversion" relation and "group" principle [*Matthies et al.*, 2001]. The GMS algorithm based on *Eshelby's* [1957] inclusion model in a homogenous matrix is more convincing from a purely physical point of view because it imposes clear stress-strain relationships for grains approximated by ellipsoidal inclusions. We treat DEM units as single crystals of spherical shape, and we consider that other minerals involved (quartz, pyrite, albite) have spherical shape. In this case, GEO elements included into GMS algorithm do not change the solution for elastic constants, since for a mixture of spherical constituents both p- and q-branches (equations (9) and (10)) converge to the same result. Thus, it is not the origin of differences between models using GMS and GEO averaging methods in Table 8 (e.g., #4 and #5).

[120] From a microstructural point of view, even the approximation of grains and pores by ellipsoidal shapes (Figure 13) does not correspond to reality as illustrated by TEM/SEM (Figures 1 and 4). Local stress concentrations and nonuniform stress fields could change the elastic behavior of the polycrystal. To address issues of local topology and short-range heterogeneities, finite element methods should be considered [e.g., *Radtke et al.*, 2010], and a fast Fourier transform-based approach [e.g., *Lebensohn et al.*, 2011] seems to be promising. But here additional difficulties arise in experimental quantification of position and orientation correlations in complex textured multiphase materials as shales.

[121] In conclusion, we want to quote *Watt et al.* [1976]: "As is true in the statistical treatment, when applying approximations we are faced with the problem of relating the specific mathematical approximation to the physical characteristics of real materials." This view is relevant in the context of shale elastic properties models. We propose two different models using the same input parameters (Figure 11) that produce similar results within margins of experimental uncertainties. To demonstrate that that these models reflect the actual physics behind the shale microstructure, and are not just numeric artifacts satisfying mathematical conditions, requires further efforts.

6.   Conclusions

[122] This is one of the first studies that models elastic anisotropy of shale based on measured microstructural features and compares model results with experimentally determined elastic properties. SEM, TEM, X-ray diffraction, and microtomography experiments have been performed to quantify composition, texture, and microstructure of a Kimmeridge shale. Based on these data, several methods have been applied to calculate elastic properties of shale to highlight dependencies of elastic constants on different model parameters. The shape of crystallites and pores, their volume fractions, and their orientation distributions play important roles in models. We have shown that different models can explain experimental elastic constants within estimated error margins. The model using only self-consistent averaging seems physically more justified and provides a satisfactory solution with lower pore volume. The models should now be applied to shales with different microstructures, particularly pore structures, to further test their applicability.

References

Aleksandrov, K. S., and T. V. Ryzhova (1961), The elastic properties of rock-forming minerals. II: Layered silicates, Izv. Acad. Sci. USSR, *Geophys. Ser.*, *12*, 1799–1804.

Almqvist, B. S. G., D. Mainprice, C. Madonna, L. Burlini, and A. M. Hirt (2011), Application of differential effective medium, magnetic pore fabric analysis, and X-ray microtomography to calculate elastic properties of porous and anisotropic rock aggregates, *J. Geophys. Res.*, *116*, B01204, doi:10.1029/2010JB007750.

Antao, S. M., I. Hassan, J. Wang, P. L. Lee, and B. H. Toby (2008), State-of-the-art high-resolution powder X-ray diffraction (HRPXRD) illustrated with Rietveld structure refinement of quartz, sodalite, tremolite, and meionite, *Can. Mineral.*, *46*, 1501–1509.

Aplin, A. C., and S. R. Larter (2005), Fluid flow, pore pressure, wettability and leakage in mudstone cap rocks, in *Evaluating Fault and Cap Rock Seals*, American Association of Petroleum Geologists Hedberg Series No.2, edited by P. Boult, and J. Kaldi, pp. 1-12, AAPG, Tulsa, OK.

Arns, C. H., M. A. Knackstedt, W. Val Pinczewski, and E. J. Garboczi (2002), Computation of linear elastic properties from microtomographic images: Methodology and agreement between theory and experiment, *Geophysics*, *67*, 1396–1405.

Aste, T. (1996), Circle, sphere and drop packings, *Phys. Rev. E*, *53*, 2571–2579.

Bailey, S. W. (Ed) (1984), *Micas, Rev. in Mineral.*, vol. *13*, Mineral. Soc. of Am., Washington, D. C.

Bayuk, I. O., M. Ammerman, and E. M. Chesnokov (2007), Elastic moduli of anisotropic clay, *Geophysics*, *72*, D107–D117.

Ben Ismail, W., and D. Mainprice (1998), An olivine fabric database: An overview of upper mantle fabrics and seismic anisotropy, *Tectonophysics*, *296*, 145–157.

Berryman, J. G. (1980a), Long-wavelength propagation in composite elastic media I. Spherical inclusions, *J. Acoust. Soc. Am.*, *68*, 1809–1819.

Berryman, J. G. (1980b), Long-wavelength propagation in composite elastic media II. Ellipsoidal inclusions, *J. Acoust. Soc. Am.*, *68*, 1820–1831.

Bish, D. L., and R. B. Von Dreele (1989), Rietveld refinement of non-hydrogen atomic positions in kaolinite, *Clays Clay Miner.*, *37*, 289–296.

Bóna, A., D. Nadri, and M. Brajanovski (2012), Thomsen's parameters from P-wave measurements in a spherical sample, *Geophys. Prospect.*, *60*, 103–116.

Bossart, P., and M. Thury (2007), Research in the Mont Terri Rock laboratory: Quo vadis?, *Phys. Chem. Earth Part A.*, *32*, 19–31.

Brown, J. M., E. H. Abramson, and R. J. Angel (2006), Triclinic elastic constants for low albite, *Phys. Chem. Miner.*, *33*, 256–265.

Bruggeman, D. A. G. (1935), Berechnung verschiedener physikalischer Konstanten von heterogenen Substanzen. I. Dielektrizitätskonstanten und

Leitfähigkeiten der Mischkörper aus isotropen Substanzen, *Ann. Phys.*, *24*, 636–679.

Budiansky, B. (1965), On the elastic moduli of some heterogeneous materials, *J. Mech. Phys. Solids*, *13*, 223–227.

Bunge, H.-J. (1982), *Texture Analysis in Materials Science: Mathematical Methods*, Butterworths, London.

Castagna, J. P., M. L. Batzle, and T. K. Kan (1993), Rock physics—The link between rock properties and AVO response, in *Offset-Dependent Reflectivity—Theory and Practice of AVO Analysis*, edited by J. P. Castagna, and M. M. Backus, pp. 135–171, Society of Exploration Geophysicists, Tulsa, Okla.

Chadwick, R. A., P. Zweigel, U. Gregersen, G. A. Kirby, S. Holloway, and P. N. Johannessen (2004), Geological reservoir characterization of a CO_2 storage site: The Utsira Sand, Sleipner, northern North Sea, *Energy*, *29*, 1371–1381.

Cholach, P. Y., and D. R. Schmitt (2006), Intrinsic elasticity of a textured transversely isotropic muscovite aggregate: Comparisons to the seismic anisotropy of schists and shales, *J. Geophys. Res.*, *111*, B09410, doi:10.1029/2005JB004158.

Dellinger, J., and L. Vernik (1994), Do traveltimes in pulse-transmission experiments yield anisotropic group or phase velocities?, *Geophysics*, *59*, 1774–1779.

Dewhurst, D. N., and A. F. Siggins (2006), Impact of fabric microcracks and stress field on shale anisotropy, *Geophys. J. Int.*, *165*, 135–148.

Downs, R. T., R. M. Hazen, and L. W. Finger (1994), The high-pressure crystal chemistry of low albite and the origin of the pressure dependency of Al-Si ordering, *Am. Mineral.*, *79*, 1042–1052.

Dræge, A., M. Jakobsen, and T. A. Johansen (2006), Rock physics modelling of shale diagenesis, *Pet. Geosci.*, *12*, 49–57.

Eshelby, J. D. (1957), The determination of the elastic field of an ellipsoidal inclusion, and related problems, *Proc. R. Soc. London, Ser. A*, *241*, 376–396.

Gualtieri, A. F. (2000), Accuracy of XRPD QPA using the combined Rietveld-RIR method, *J. Appl. Crystallogr.*, *33*, 267–278.

Hashin, Z., and S. Shtrikman (1963), A variational approach to the theory of the elastic behaviour of multiphase materials, *J. Mech. Phys. Solids*, *11*, 127–140.

Hayward, A. T. J. (1967), Compressibility equations for liquids: A comparative study, *Br. J. Appl. Phys.*, *18*, 965–977.

Heyliger, P., H. Ledbetter, and S. Kim (2003), Elastic constants of natural quartz, *J. Acoust. Soc. Am.*, *114*, 644–650.

Hill, R. (1952), The elastic behaviour of a crystalline aggregate, *Proc. Phys. Soc. London, Sect. A*, *65*, 349–354.

Hill, R. (1965), A self-consistent mechanics of composite materials, *J. Mech. Phys. Solids*, *13*, 213–222.

Hirsekorn, S. (1990), Elastic properties of polycrystals—A review, *Texture Microstruct.*, *12*, 1–14.

Hornby, B. E. (1998), Experimental laboratory determination of the dynamic elastic properties of wet, drained shales, *J. Geophys. Res.*, *103*, 29945–29964.

Hornby, B. E., L. M. Schwartz, and J. A. Hudson (1994), Anisotropic effective-medium modeling of the elastic properties of shales, *Geophysics*, *59*, 1570–1583.

Jakobsen, M., and T. A. Johansen (2000), Anisotropic approximations for mudrocks: A seismic laboratory study, *Geophysics*, *65*, 1711–1725.

Jakobsen, M., J. A. Hudson, T. A. Minshull, and S. C. Singh (2000), Elastic properties of hydrate-bearing sediments using effective medium theory, *J. Geophys. Res.*, *105*, 561–577.

Jakobsen, M., T. A. Johansen, and B. O. Ruud (2001), Modeled velocity and reflectivity properties of anisotropic hydrated sediments, *J. Comput. Acoust.*, *9*, 1507–1522.

Jech, J. (1991), Computation of elastic parameters of anisotropic medium from travel times of quasi-compressional waves, *Phys. Earth Planet. Inter.*, *66*, 153–159.

Johansen, T. A., B. O. Ruud, and M. Jakobsen (2004), Effect of grain scale alignment on seismic anisotropy and reflectivity of shales, *Geophys. Prospect.*, *52*, 133–149.

Johnston, D. H. (1987), Physical properties of shale at temperature and pressure, *Geophysics*, *52*, 1391–1401.

Jones, L. E. A., and H. F. Wang (1981), Ultrasonic velocities in Cretaceous shales from the Williston basin, *Geophysics*, *46*, 288–297.

Kanitpanyacharoen, W., D. Y. Parkinson, F. de Carlo, F. Marone, M. Stampanoni, R. Mokso, A. MacDowell, and H.-R. Wenk (2013), A comparative study of X-ray tomographic microscopy on shales at different synchrotron facilities: ALS, APS and SLS, *J. Synchrotron Radiat.*, *20*, 172–180.

Karmous, M. S. (2011), Theoretical study of kaolinite structure; energy minimization, and crystal properties, *World J. Nano Sci. Eng.*, *1*, 62–66.

Katahara, K. W. (1996), Clay mineral elastic properties, *Soc. Explor. Geophys. Tech. Program Expanded Abstr.*, *15*, 1691–1694.

Klíma, K. (1973), The computation of elastic constants of an anisotropic medium from the velocities of body waves, *Stud. Geophys. Geod.*, *17*, 115–122.

Kneer, G. (1965), Über die Berechnung der Elastizitätsmoduln vielkristalliner Aggregate mit Textur, *Phys. Status Solidi B*, *9*, 825–838.

Kröner, E. (1958), Berechnung der elastischen Konstanten des Vielkristalls aus den Konstanten des Einkristalls, *Z. Phys.*, *151*, 504–518.

Le Page, Y., and J. R. Rodgers (2005), Ab initio elasticity of FeS_2 pyrite from 0 to 135 GPa, *Phys. Chem. Miner.*, *32*, 564–567.

Le Ravalec, M., and Y. Guéguen (1996), High- and low-frequency elastic moduli for a saturated porous/cracked rock—Differential self-consistent and poroelastic theories, *Geophysics*, *61*, 1080–1094.

Lebensohn, R. A., A. D. Rollett, and P. Suquet (2011), Fast Fourier transform-based modeling for the determination of micromechanical fields in polycrystals, *J. Miner. Met. Mater. Soc. (JOM)*, *63*, 13–18.

Liu, Y., and D. R. Schmitt (2006), The transition between the scale domains of ray and effective medium theory and anisotropy: Numerical models, *Pure Appl. Geophys.*, *163*, 1327–1349.

Lokajicek, T., P. Lukas, A. N. Nikitin, I. V. Papushkin, V. V. Sumin, and R. N. Vasin (2011), The determination of the elastic properties of an anisotropic polycrystalline graphite using neutron diffraction and ultrasonic measurements, *Carbon*, *49*, 1374–1384.

Lonardelli, I., H.-R. Wenk, and Y. Ren (2007), Preferred orientation and elastic anisotropy in shales, *Geophysics*, *72*, D33–D40.

Lutterotti, L., S. Matthies, H.-R. Wenk, A. S. Schultz, and J. W. Richardson (1997), Combined texture and structure analysis of deformed limestone from time-of-flight neutron diffraction spectra, *J. Appl. Phys.*, *81*, 594–600.

Lutterotti, L., D. Chateigner, S. Ferrari, and J. Ricote (2004), Texture, residual stress and structural analysis of thin films using a combined X-ray analysis, *Thin Solid Films*, *450*, 34–41.

Lutterotti, L., M. Voltolini, H.-R. Wenk, K. Bandyopadhyay, and T. Vanorio (2010), Texture analysis of turbostratically disordered Ca-montmorillonite, *Am. Mineral.*, *95*, 98–103.

Makarynska, D., B. Gurevich, R. Ciz, C. H. Arns, and M. A. Knackstedt (2008), Finite element modelling of the effective elastic properties of partially saturated rocks, *Comput. Geosci.*, *34*, 647–657.

Mallants, D., J. Marivoet, and X. Sillen (2001), Performance assessment of the disposal of vitrified high-level waste in a clay layer, *J. Nucl. Mater.*, *298*, 125–135.

Manevitch, O. L., and G. C. Rutledge (2004), Elastic properties of a single lamella of montmorillonite by molecular dynamics, *J. Phys. Chem. B*, *108*, 1428–1435.

Matthies, S. (2002), 20 years WIMV, history, experience and contemporary developments, *Mater. Sci. Forum*, *408-412*, 95–100.

Matthies, S. (2005), The ODF-spectrum: A new and comprehensive characterization of the degree of anisotropy of orientation distributions, *Mater. Sci. Forum*, *495-497*, 331–338.

Matthies, S. (2010), On the combination of self-consistent and geometric mean elements for the calculation of the elastic properties of textured multi-phase samples, *Solid State Phenom.*, *160*, 87–93.

Matthies, S. (2012), GEO-MIX-SELF calculations of the elastic properties of a textured graphite sample at different hydrostatic pressures, *J. Appl. Crystallogr.*, *45*, 1–16.

Matthies, S., and M. Humbert (1995), On the principle of a geometric mean of even-rank symmetric tensors for textured polycrystals, *J. Appl. Crystallogr.*, *28*, 254–266.

Matthies, S., and G. W. Vinel (2005), On the calculation of the Eshelby tensor and the beauty of our nature, *Solid State Phenom.*, *105*, 113–120.

Matthies, S., and H.-R. Wenk (2009), Transformations for monoclinic crystal symmetry in texture analysis, *J. Appl. Crystallogr.*, *42*, 564–571.

Matthies, S., H.-R. Wenk, and G. W. Vinel (1988), Some basic concepts of texture analysis and comparison of three methods to calculate orientation distributions from pole figures, *J. Appl. Crystallogr.*, *21*, 285–304.

Matthies, S., H. G. Priesmeyer, and M. R. Daymond (2001), On the diffractive determination of single-crystal elastic constants using polycrystalline samples, *J. Appl. Crystallogr.*, *34*, 585–601.

Mazo, M. A., L. I. Manevitch, E. B. Gusarova, M. Y. Shamaev, A. A. Berlin, N. K. Balabaev, and G. C. Rutledge (2008a), Molecular dynamics simulation of thermomechanical properties of montmorillonite crystal. I. Isolated clay nanoplate, *J. Phys. Chem. B*, *112*, 2964–2969.

Mazo, M. A., L. I. Manevitch, E. B. Gusarova, M. Y. Shamaev, A. A. Berlin, N. K. Balabaev, and G. C. Rutledge (2008b), Molecular dynamics simulation of thermomechanical properties of montmorillonite crystal. II. Hydrate montmorillonite crystal, *J. Phys. Chem. C*, *112*, 17056–17062.

Militzer, B., H.-R. Wenk, S. Stackhouse, and L. Stixrude (2011), First-principles calculation of the elastic moduli of sheet silicates and their application to shale anisotropy, *Am. Mineral.*, *96*, 125–137.

Milton, G. W., and R. V. Kohn (1988), Variational bounds on the effective moduli of anisotropic composites, *J. Mech. Phys. Solids*, *36*, 597–629.

Morris, P. R. (1970), Elastic constants of polycrystals, *Int. J. Eng. Sci.*, *8*, 49–61.

Moyano, B., K. T. Spikes, T. A. Johansen, and N. H. Mondol (2012), Modeling compaction effects on the elastic properties of clay-water composites, *Geophysics*, *77*, D171–D183.

Mukerji, T., G. Mavko, D. Mujica, and N. Lucet (1995), Scale-dependent seismic velocity in heterogeneous media, *Geophysics*, *60*, 1222–1233.

Nadri, D., J. Sarout, A. Bóna, and D. Dewhurst (2012), Estimation of anisotropy parameters of transversely isotropic shales with a tilted symmetry axis, *Geophys. J. Int.*, *190*, 1197–1203.

Nishizawa, O. (1982), Seismic velocity anisotropy in a medium containing oriented cracks—Transversely isotropic case, *J. Phys. Earth*, *30*, 331–347.

Nishizawa, O., and K. Kanagawa (2010), Seismic velocity anisotropy of phyllosilicate-rich rocks: characteristics inferred from experimental and crack-model studies of biotite-rich schist, *Geophys. J. Int.*, *182*, 375–388.

Nishizawa, O., and T. Yoshino (2001), Seismic velocity anisotropy in mica-rich rocks: An inclusion model, *Geophys. J. Int.*, *145*, 19–32.

Nye, J. F. (1985), *The Physical Properties of Crystals: Their Representation by Tensors and Matrices*, Oxford University Press, Oxford.

O'Connell, R. J., and B. Budiansky (1974), Seismic velocities in dry and saturated cracked solids, *J. Geophys. Res.*, *79*, 5412–5426.

Ohno, I., K. Harada, and C. Yoshitomi (2006), Temperature variation of elastic constants of quartz across the α-β transition, *Phys. Chem. Miner.*, *33*, 1–9.

Ortega, A. J., F.-J. Ulm, and Y. Abousleiman (2007), The effect of nanogranular nature of shale on their poroelastic behavior, *Acta Geotech.*, *2*, 155–182.

Pham, N. H., J. M. Carcione, H. B. Helle, and B. Ursin (2002), Wave velocities and attenuation of shaley sandstones as a function of pore pressure and partial saturation, *Geophys. Prospect.*, *50*, 615–627.

Plançon, A., S. I. Tsipurski, and V. A. Drits (1985), Calculation of intensity distribution in the case of oblique texture electron diffraction, *J. Appl. Crystallogr.*, *18*, 191–196.

Ponte Castañeda, P., and J. R. Willis (1995), The effect of spatial distribution on the effective behavior of composite materials and cracked media, *J. Mech. Phys. Solids*, *43*, 1919–1951.

Radtke, F. K. F., A. Simone, and L. J. Sluys (2010), A partition of unity finite element method for obtaining elastic properties of continua with embedded thin fibers, *Int. J. Numer. Methods Eng.*, *84*, 708–732.

Reuss, A. (1929), Berechnung der Fließgrenze von Mischkristallen auf Grund der Plastizitätsbedingung für Einkristalle, *Z. Angew. Math. Mech.*, *9*, 49–58.

Rieder, M., J. C. Crelling, O. Šustai, M. Drábek, Z. Weiss, and M. Klementová (2007), Arsenic in iron disulfides in a brown coal from the North Behemian Basin, Czech Republic, *Int. J. Coal Geol.*, *71*, 115–121.

Rietveld, H. M. (1969), A profile refinement method for nuclear and magnetic structures, *J. Appl. Crystallogr.*, *2*, 65–71.

Rundle, J. B., and K. W. Schuler (1981), A composite model for the anisotropic elastic moduli of lean oil shale, *Geophysics*, *46*, 163–171.

Sato, H., K. Ono, C. T. Johnston, and A. Yamagishi (2005), First-principle studies on the elastic constants of a 1:1 layered kaolinite mineral, *Am. Mineral.*, *90*, 1824–1826.

Sayers, C. M. (1994), The elastic anisotropy of shales, *J. Geophys. Res.*, *99*, 767–774.

Sayers, C. M. (2008), The effect of low aspect ratio pores on the seismic anisotropy of shales, *Soc. Explor. Geophys. Tech. Program Expand. Abstr.*, *27*, 2750–2754.

Schoenberg, M., and J. Douma (1988), Elastic wave propagation in media with parallel fractures and aligned cracks, *Geophys. Prospect.*, *36*, 571–590.

Silva, M. B. C., and A. Stovas (2009), Correspondence between the low- and high-frequency limits for anisotropic parameters in a layered medium, *Geophysics*, *74*, WA25–WA33.

Spalthoff, P., W. Wunnike, C. Nauer-Gerhard, H.-J. Bunge, and E. Schneider (1993), Determination of the elastic tensor of a textured low-carbon steel, *Texture Microstruct.*, *21*, 3–16.

Spikes, K. T. (2011), Modeling elastic properties and assessing uncertainty of fracture parameters in the Middle Bakken Siltstone, *Geophysics*, *76*, E117–E126.

Srinivasan, K. R., K. Matouš, and P. H. Geubelle (2008), Generalized finite element method for modeling nearly incompressible bimaterial hyperelastic solids, *Comput. Meth. Appl. Mech. Eng.*, *197*, 4882–4893.

Suter, J. L., P. V. Coveney, H. C. Greenwell, and M.-A. Thyveetil (2007), Large-scale molecular dynamics study of montmorillonite clay: Emergence of undulatory fluctuations and determination of material properties, *J. Phys. Chem. C*, *111*, 8248–8259.

Tissot, B. P., and D. H. Welte (1984), *Petroleum Formation and Occurrence*, Springer, Berlin.

Twardowski, K., J. Traple, and S. Rychlicki (2004), Evaluation of rock porosity measurement accuracy with a helium porosimeter, *Acta Montan. Slovaca*, *9*, 316–318.

Ufer, K., G. Roth, R. Kleeberg, H. Stanjek, R. Dohrmann, and J. Bergmann (2004), Description of X-ray powder pattern of turbostratically disordered layer structures with a Rietveld compatible approach, *Z. Kristallogr.*, *219*, 519–527.

Valcke, S. L. A., M. Casey, G. E. Lloyd, J.-M. Kendall, and Q. J. Fisher (2006), Lattice preferred orientation and seismic anisotropy in sedimentary rocks, *Geophys. J. Int.*, *166*, 652–666.

Vaughan, M. T., and S. Guggenheim (1986), Elasticity of muscovite and its relationship to crystal structure, *J. Geophys. Res.*, *91*, 4657–4664.

Vernik, L., and X. Liu (1997), Velocity anisotropy in shales: A petrophysical study, *Geophysics*, *62*, 521–532.

Vilhelm, J., V. Rudajev, R. Živor, T. Lokajíček, and Z. Pros (2010), Influence of crack distribution of rocks on P-wave velocity anisotropy— A laboratory and field scale study, *Geophys. Prospect.*, *58*, 1099–1110.

Voigt, W. (1887), *Theoretische Studien über die Elasticitätsverhältnisse der Krystalle*, Dieterichsche Verlags-Buchhandlung, Göttingen.

Walpole, L. J. (1969), On the overall elastic moduli of composite materials, *J. Mech. Phys. Solids*, *17*, 235–251.

Walsh, J. B. (1965), The effect of cracks on the compressibility of rocks, *J. Geophys. Res.*, *70*, 381–389.

Wang, Z., H. Wang, and M. E. Cates (2001), Effective elastic properties of solid clays, *Geophysics*, *66*, 428–440.

Watt, J. P., G. F. Davies, and R. J. O'Connell (1976), The elastic properties of composite materials, *Rev. Geophys. Space Phys.*, *14*, 541–563.

Wenk, H.-R., S. Matthies, J. Donovan, and D. Chateigner (1998), BEARTEX: A Windows-based program system for quantitative texture analysis, *J. Appl. Crystallogr.*, *31*, 262–269.

Wenk, H.-R., et al. (2013), Rietveld texture analysis from synchrotron diffraction images: II. Complex multiphase materials and diamond anvil cell experiments, *Powder Diffraction*, in press.

Wenk, H.-R., M. Voltolini, H. Kern, T. Popp, and M. Mazurek (2008), Anisotropy in shale from Mont Terri, *Leading Edge*, *27*, 742–748.

Wenk, H.-R., W. Kanitpanyacharoen, and M. Voltolini (2010), Preferred orientation of phyllosilicates: Comparison of fault gouge, shale and schist, *J. Struct. Geol.*, *32*, 478–489.

Wenk, H.-R., R. N. Vasin, H. Kern, S. Matthies, S. C. Vogel, and T. I. Ivankina (2012), Revisiting elastic anisotropy of biotite gneiss from the Outokumpu scientific drill hole based on new texture measurements and texture-based velocity calculations, *Tectonophysics*, *570-571*, 123–134.

Wirth, R. (2009), Focused Ion Beam (FIB) combined with SEM and TEM: Advanced analytical tools for studies of chemical composition, microstructure and crystal structure in geomaterials on a nanometre scale, *Chem. Geol.*, *261*, 217–229.